Check for updates

JGR Solid Earth

RESEARCH ARTICLE
10.1029/2020JB021168

Growth of Collisional Orogens From Small and Cold to Large and Hot—Inferences From Geodynamic Models

Sebastian G. Wolf[1], Ritske S. Huismans[1], Josep-Anton Muñoz[2], Magdalena Ellis Curry[3,4], and Peter van der Beek[3,5]

[1]Department of Earth Science, Bergen University, Bergen, Norway, [2]Geomodels Research Institute, University of Barcelona, Barcelona, Spain, [3]CNRS, ISTerre, Université Grenoble Alps, Grenoble, France, [4]Department of Earth and Atmospheric Sciences, University of Houston, Houston, TX, USA, [5]Insitut für Geowissenschaften, Universität Potsdam, Potsdam, Germany

Key Points:

- Coupled thermo-mechanical-surface-process models are used to investigate orogenic growth from small and cold to large and hot
- Models give insight into typical shortening distribution and structural style of growing mountain belts
- Comparison to Pyrenees, Alps, and Himalaya-Tibet highlights key similarities and differences between models and natural examples

Supporting Information:

- Supporting Information S1
- Movie S1
- Movie S2
- Movie S3
- Movie S4
- Movie S5
- Movie S6
- Movie S7
- Movie S8
- Movie S9

Correspondence to:
S. G. Wolf,
sebastian.wolf@uib.no

Citation:
Wolf, S. G., Huismans, R. S., Muñoz, J.-A., Curry, M. E., & van der Beek, P. (2021). Growth of collisional orogens from small and cold to large and hot—inferences from geodynamic models. *Journal of Geophysical Research: Solid Earth*, *126*, e2020JB021168. https://doi.org/10.1029/2020JB021168

Received 12 OCT 2020
Accepted 2 DEC 2020

© 2020. The Authors.
This is an open access article under the terms of the Creative Commons Attribution NonCommercial License, which permits use, distribution and reproduction in any medium, provided the original work is properly cited and is not used for commercial purposes.

Abstract It is well documented that the interplay between crustal thickening and surface processes determines growth of continent-continent collision orogens from small and cold to large and hot. Additionally, studies have demonstrated that the structural style of a mountain belt is strongly influenced by inherited (extensional) structures, the pattern of erosion and deposition, as well as the distribution of shallow detachment horizons. However, the factors controlling distribution of shortening and variable structural style as a function of convergence and surface process efficiency remain less explored. We use a 2D upper-mantle scale plane-strain thermo-mechanical model (FANTOM) coupled to a planform, mass conserving surface-process model (Fastscape), to investigate the long-term evolution of mountain belts and the influence of lithospheric pull, extensional inheritance, surface processes efficiency, and decoupling between thin-and thick-skinned tectonics. We establish an evolutionary shortening distribution for orogenic growth from a mono-vergent wedge to an orogenic plateau, and find that internal crustal loading is the main factor controlling the large scale evolution, while lithospheric pull modulates the plate driving force for orogenesis. Limited foreland-basin filling and minor exhumation of the orogen core are characteristic for low surface-process efficiency, while thick foreland-basin fill, and profound exhumation of the orogen core are characteristic for high surface-process efficiency. Utilizing a force balance analysis, we show how inherited structures, surface processes, and decoupling between thin- and thick-skinned deformation influence structural style during orogenic growth. Finally, we present a comparison of our generic modeling results with natural systems, with a particular focus on the Pyrenees, Alps, and Himalaya-Tibet.

1. Introduction

Continent-continent collision creates mountain belts that grow in size with increasing amounts of plate convergence. Orogenic temperature is directly related to the amount of crustal thickening by horizontal shortening, as heat producing elements are concentrated in upper and middle crustal rocks (e.g., Hacker et al., 2015). Crustal heating, in turn, has a weakening effect on crustal rheology and controls regional metamorphism; influencing mountain-belt structure and deformation. During orogenic growth, surface processes shape mountain-belt topography, fill the evolving foreland basins and exhume metamorphic rocks. In the end-member case, erosion may even fully balance orogenic growth, creating a flux steady state between tectonics and erosion (Stolar et al., 2007; Willett & Brandon, 2002). Beaumont et al. (2006) propose a temperature-magnitude relationship for orogenic growth from small and cold to large and hot, in analogy to the Hertzsprung-Russel diagram of stellar classification. The temperature-magnitude diagram, however, does not explain whether there is a characteristic distribution of shortening and structural style (e.g., thin- and thick-skinned deformation, thrusting style) as a function of orogen size, and its controlling factors. In this study, we use thermo-mechanical models that are fully coupled to a landscape-evolution model, to investigate the first-order factors controlling the distribution of shortening and the different structural styles related to orogenic growth from small and cold to large and hot during continent-continent collision.

A typical example of a small and cold orogen is the Pyrenean mountain belt, which grew by inversion of a rift system with additional crustal shortening and plate convergence of at most 165 km (Beaumont et al., 2000; Muñoz, 1992). The Alps, an intermediate size orogen, have a more complex history, that includes

subduction, ultra-high-pressure (UHP)-rock exhumation, passive margin inversion and terrane accretion preceding continent-continent collision. Crustal shortening is difficult to estimate and variable along strike but certainly exceeds 150 km in the west-central part (Schmid & Kissling, 2000; Schmid et al., 1996, 2017). The only modern large and hot, continent-continent collision system with an orogenic plateau is the Himalayan-Tibetan orogen. This mountain belt is characterized by a hot, and viscously weak middle crust on top of a flat Moho, and formed in its recent state by collision between India and Eurasia with postcollision convergence estimated to be larger than 2000 km (Negredo et al., 2007). Continent-continent collision was preceded by oceanic subduction and accretion of small continental masses at the Asian margin, which today are partly underlain by metasomatized or highly thinned lithospheric mantle (Chung et al., 2005; Owens & Zandt, 1997).

These three examples show that continent-continent collision is often preceded by passive margin inversion, subduction of oceanic lithosphere, and/or terrane accretion. Hence, continent-continent collision of plates with normal crustal thickness is typically preceded by a heterogeneous shortening phase, which includes inversion of inherited structures. Despite their differences, the three type-examples presented above have important first order similarities: The Pyrenees, Alps, and Himalayas have thin-skinned foreland fold-thrust belts, fed partly by syn-contractional sediments, which are detaching in weak décollement horizons (DeCelles et al., 2001; Muñoz, 1992; Robinson, 2008; Sommaruga, 1999). Furthermore, crustal material detaches on top of the lower crust to form thick-skinned thrust sheets, and the lithospheric mantle and lower crust of one plate subduct into the underlying upper mantle. This separates the downgoing pro-plate from the overriding retro-plate at a mantle singularity, also termed "S-point" (Willett et al., 1993). During continent-continent collision, the pull exerted by the subducting pro-lithosphere is dependent on its degree of chemical depletion (Griffin et al., 1998; Poudjom Djomani et al., 2001), and can be augmented by the pull of an oceanic slab, in cases in which it remains attached to the downgoing continental lithospheric mantle. Slab pull, developing from subducting oceanic lithosphere, provides a first-order control on plate movement on Earth (Forsyth & Uyeda, 1975). Similarly, the pull of the subducting lithospheric mantle during continent-continent collision has the potential to strongly influence the tectonic forces required to drive plate convergence and thus orogeny (Becker & Faccenna, 2011; Capitanio et al., 2010; Cloos, 1993). However, no studies have yet specifically investigated the influence of lithospheric pull on structure, deformation, and the resulting tectonic forces in growing mountain belts.

Subduction of the lithospheric mantle motivated early crustal-scale numerical models with a kinematically controlled velocity discontinuity (S-point, Beaumont et al., 1994, 1999, 2001, 2006; Braun & Beaumont, 1995; Vanderhaeghe et al., 2003; Willett & Beaumont, 1994; Willett et al., 1993). These models investigated, among others, how much the subducting pro-plate respectively the overlying retro-plate contribute to crustal thickening (Beaumont et al., 1999; Ellis & Beaumont, 1999; Vanderhaeghe et al., 2003; Willett, 1999; Willett & Beaumont, 1994; Willett et al., 1993). They showed that there can be different modes of pro-and retro-wedge deformation, elegantly described in terms of the PURCE framework (P, R = pro-, retro-side, U = uplifted plug, C = subduction channel, E = elevated plateau, Beaumont et al., 1999; Jamieson & Beaumont, 2013). More specifically, already the earliest S-point models showed a characteristic deformation pattern involving pro-and retro-side crust and movement of the orogen onto the retro-side as function of orogen size (Beaumont et al., 1994; Willett, 1999; Willett & Beaumont, 1994). In contrast, the next generation of upper-mantle scale numerical models with self-consistent lithospheric subduction showed that a weak overriding plate might be prerequisite for retro-plate deformation (J. P. Butler et al., 2011), or that extensional inheritance might be the main factor controlling retro-plate deformation during continent-continent collision (Erdős et al., 2014). The discrepancy between results obtained with different modeling methods and setups indicates that the factors controlling pro-and retro-wedge deformation in growing continent-continent collision orogens are not fully understood and require explanation.

It has long been shown that there is a strong feedback between surface processes and tectonics, where high erosional efficiency can lead to a steady state between tectonic material influx and erosional outflux of material (Beaumont et al., 1992, 2001; Hilley et al., 2004; Stolar et al., 2007; Whipple & Meade, 2004, 2006; Willett, 1999; Willett & Brandon, 2002). Understanding the interplay between surface processes and tectonics has historically been approached from either a surface-process perspective (e.g., Hilley et al., 2004; Stolar et al., 2007; Whipple & Meade, 2004; Whipple & Tucker, 1999), assuming simplified deformation

and omitting deposition, or from a tectonic perspective, using simplified surface processes (e.g., Beaumont et al., 2001; Erdős et al., 2014, 2015; Grool et al., 2019). New surface-process algorithms (Braun & Willett, 2013; Yuan et al., 2019) and high resolution thermo-mechanical tectonic models (Andrews & Billen, 2009; Erdős et al., 2014; Ruh et al., 2017; Thieulot, 2011; Ueda et al., 2015) facilitate the first investigations into the full coupling between landscape evolution, erosion, sedimentation, and tectonics. This advancement not only bridges the gap between surface processes and tectonics, but also permits investigation into the interaction between thin- and thick-skinned deformation during orogenic growth, which previously has been investigated separately (e.g., Fillon et al., 2013; Stockmal et al., 2007).

Here, we investigate whether there is a common relationship between mountain-belt size, distribution of deformation, and structural style in terms of thin-versus thick-skinned deformation, thrust spacing, influence of inherited weaknesses, and consequences of surface processes, and are particularly driven to understand the underlying physical controls. To that end we use high-resolution 2D thermo-mechanical forward models coupled to a 2D, mass-conserving surface process model and investigate the influences of slab pull, extensional inheritance, surface-process efficiency, and decoupling of the foreland-fold-thrust belts on the growth of continent-continent collision orogens from small and cold to large and hot. To find key similarities and differences between our modeling results and mountain belts on Earth, we compare model inferences with the three orogens introduced above: The Pyrenees, Alps, and Himalayan-Tibetan orogen.

2. Methodology

2.1. Model Design

We use the thermo-mechanically coupled 2D finite element code FANTOM to model mountain building (Thieulot, 2011; Wolf & Huismans, 2019, see Appendixes A1 and A2). The initial model geometry represents a 1,200 km wide and 600 km deep, idealized, crustal and upper mantle cross-section (Figure 1, Table 1). It consists of a laterally uniform continental lithosphere with 35 km thick crust, 85 km thick lithospheric mantle, and sublithospheric upper mantle down to the lower model boundary. Crustal material is subdivided into predeformation sedimentary rocks on top of a mechanically weak horizon acting as a future décollement for thin-skinned thrusts (from here on referred to as décollement horizon), followed by upper- and mid-crust to 25 km depth, and lower crust to 35 km depth. All materials have the same frictional-plastic parameters affected by strain weakening, apart from the décollement below the predeformation sedimentary rocks. The latter is represented by an effective angle of internal friction $\phi_{\text{eff}} = 2°$ and cohesion $C = 4$ MPa, which corresponds to fully strain weakened material. This layer allows for the evolution of a thin-skinned fold-thrust belt. In model M7 (see Table 2) we test the influence of a very weak décollement horizon with fixed viscosity of 1×10^{19} Pa s, mimicking a salt layer at shallow depth. The terms thin-skinned and thick-skinned deformation are used throughout the manuscript to describe whether thrusts originate in the weak décollement horizon or in the viscous middle crust.

Viscous flow of upper and mid crustal materials follows a wet quartz flow law (Gleason & Tullis, 1995), and the lower crust is represented by a dry Maryland diabase flow law (Mackwell et al., 1998). Lithospheric mantle is based on a wet olivine flow law (Karato & Wu, 1993), scaled by a factor $f = 5$ to represent dry- and melt-depleted conditions, and the sublithospheric mantle follows the wet olivine flow law scaled by $f = 1$. Lithospheric mantle density depends on its degree of chemical depletion. Typical Phanerozoic mantle is 20–30 kg m^{-3} less dense, and Proterozoic mantle is typically 50 kg m^{-3} less dense than primitive mantle (Griffin et al., 1998; Poudjom Djomani et al., 2001). Depletion related density decrease of the lithospheric mantle has a strong effect on lithospheric pull and is explored in models 1 to 3 (see Table 2).

The thermal setup reflects average values (see Table 1), with a Moho temperature of 550°C and 1,330°C at the base of the lithosphere, resulting in a surface heat flow of 53 mW m^{-2} and heat flux in the sublithospheric mantle of 20.8 mW m^{-2} (Hacker et al., 2015).

The resulting rheological setup generates a viscous decoupling horizon on top of the lower crust, and coupling of the lower crust with the lithospheric mantle. This is motivated by the Pyrenees, Alps, and Himalayas which are all characterized by a viscous decoupling horizon in the middle crust and subduction of the lower crust along with the lithospheric mantle (Gao et al., 2016; Muñoz, 1992; Replumaz et al., 2010; Schmid et al., 1996).

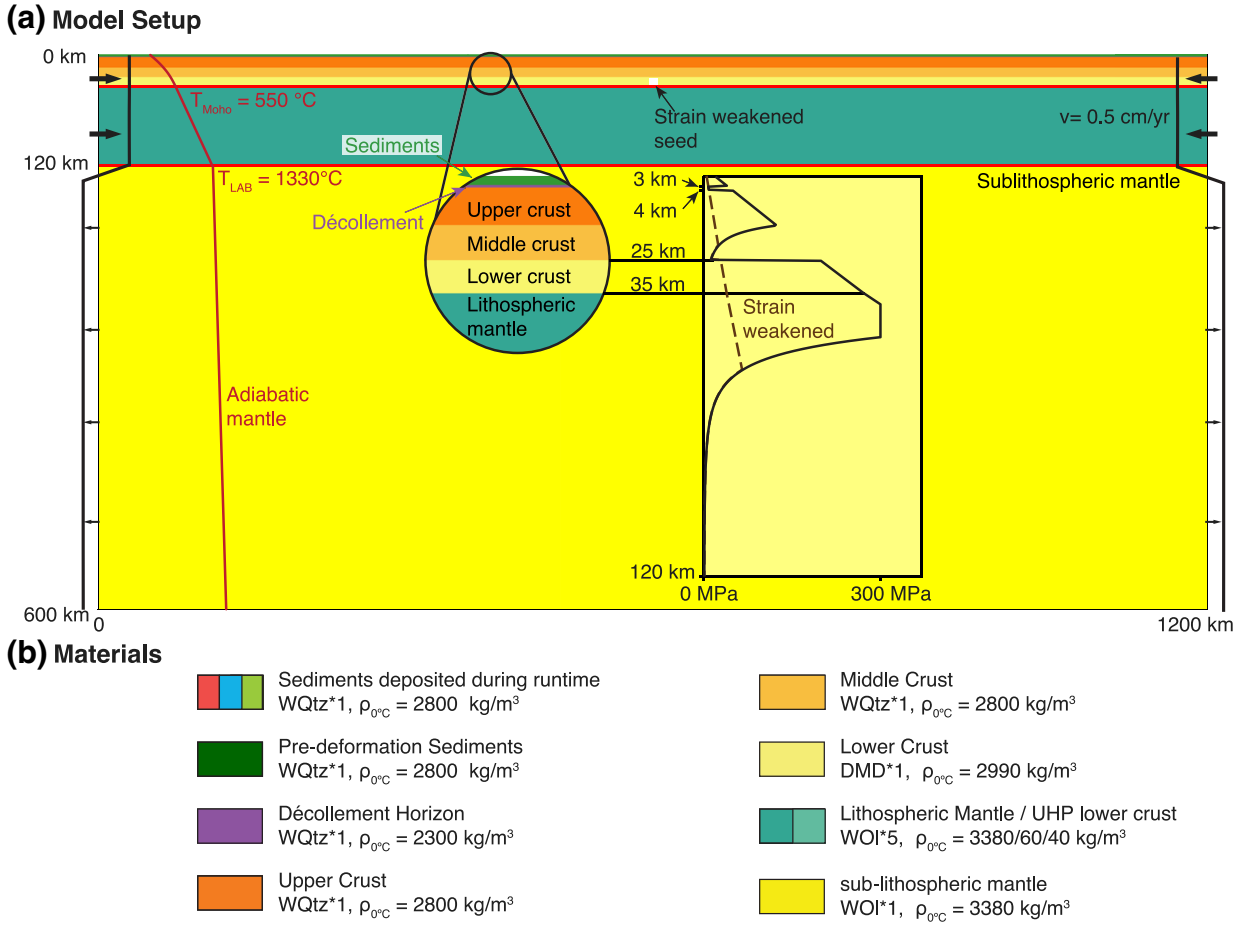

Figure 1. Model setup with (a) boundary conditions and (b) material properties. (a) The model is 1,200 km wide, 600 km deep, and has a uniform distribution of materials. Mountain building is modeled by applying an inward velocity of 0.5 cm/yr in the lithosphere on both model sides. Inflow is balanced by a small distributed outflow in the sublithospheric domain. Extension is modeled by reversing the velocity boundary conditions. The upper surface is free and the side and bottom boundaries have free-slip boundary conditions. The initial temperature profile of the continent corresponds to 1D-thermal steady state and the underlying mantle has an adiabatic gradient of 0.4°C km^{-1}. The side boundaries are insulated and the bottom boundary has a fixed temperature boundary condition of 1,522°C. The inserts show a zoom of the continental lithosphere with the corresponding initial yield-strength envelope computed with $\dot{\epsilon} = 1 \times 10^{-15} s^{-1}$. Our model materials also account for strain weakening by linearly reducing the effective angle of internal friction and cohesion as a function of strain. (b) Material description shows color, scaled flow law, and density of model materials. WQtz is the wet quartz flow law as described in Gleason and Tullis (1995), DMD is the dry Maryland flow law from Mackwell et al. (1998), and wet Ol is the wet olivine flow law from Karato and Wu (1993). The density of the lithospheric mantle is varied in Models M1 to M3.

The models include an irreversible metamorphic phase change of the strong, mafic lower continental crust at UHP-conditions, when entering the eclogite field specified in the phase diagram of Hacker (1996). For simplicity, the metamorphic equivalent has the same rheology and density as lithospheric mantle. The metamorphosed lower crust is also affected by viscous strain weakening by reducing the scaling factor f by up to 0.01 in the predefined viscous strain ($\varepsilon_{viscous}$) interval $0.1 < \varepsilon_{viscous} < 1.1$. Viscous weakening is not active at temperatures higher than 1,000°C. Viscous weakening ensures proper decoupling between the downgoing and overriding plate during the initial convergence phase, and mimics a slightly weaker plate suture zone originating for instance from preceding subduction or passive margin inversion.

Orogenesis and precollisional rifting are modeled by applying velocity boundary conditions of 0.5 cm/yr, at the model sides (see Figure 1). To localize deformation, we place a strain weakened seed in the lower crust in the model center.

The tectonic model is fully coupled to the surface process model Fastscape (Braun & Willett, 2013; Yuan et al., 2019), which computes stream-power law erosion, hillslope diffusion, and continental deposition (see Section A3). The effects of surface processes are investigated in models 5 to 7, and supplementary models

Table 1
Mechanical and Thermal Properties of the Materials

Parameters	Sedimentary rocks	Decollement horizon	Upper & middle crust	Lower crust	Mantle lithosphere	Sublithospheric mantle
Plastic rheology						
$C - C_{sw}$[a] (MPa)	20-4	4-4	20-4	20-4	20-4	20-4
$\phi_{eff} - \phi_{eff,sw}$[a] (°)	15-2	2-2	15-2	15-2	15-2	15-2
Viscous rheology						
Flow law[b]	WQtz	WQtz	WQtz	DMD	WOl	WOl
f	1	1	1	1	5	1
A (Pa $s^{1/n}$)[c]	8.57×10^{-28}	8.57×10^{-28}	8.57×10^{-28}	5.78×10^{-27}	1.76×10^{-14}	1.76×10^{-14}
n	4.0	4.0	4.0	4.7	3.0	3.0
Q (kJ mol^{-1})	223	223	223	485	430	430
V (cm^3 mol^{-1})	0	0	0	0	0	10×10^{-6}
Density						
ρ_0 (kg m^{-3})[d]	2,800	2,300	2,800	2,990	3,380/3,360/3,340 (depleted)	3,380
α (K^{-1})	3×10^{-5}	3×10^{-5}	3×10^{-5}	3×10^{-5}	3×10^{-5}	3×10^{-5}
Thermal						
k (W $m^{-1}K^{-1}$)[e]	2.25	2.25	2.25	2.25	2.25	2.25
H (μW m^{-3})	1.15	1.15	1.15	0.5	0	0
c_p (J $kg^{-1}K$)[f]	804	987	804	762	682	1,250

[a]C and ϕ_{eff} are linearly affected by strain weakening within the plastic strain interval [0.1, 1.1]. [b]WQtz is the wet quartz flow law as described in Gleason and Tullis (1995); DMD is the dry Maryland flow law from Mackwell et al. (1998); WOl is the wet olivine flow law from Karato and Wu (1993). [c]The laboratory derived preexponential flow law constant has been converted to conform with the second invariants of the stress and strain rates used in the model approach. [d]Metamorphic high pressure equivalent. The P-T-field for the metamorphic reaction coincides with the eclogite stability field from Hacker (1996). [e]Thermal conductivity for low temperatures. Between 1,335°C and 1,345°C the conductivity linearly increases from 2.25 to 52.0 Wm^{-1} K^{-1}, to mimic active mantle convection at high Nusselt number, keep the adiabatic gradient and prevent the system from cooling. [f]c_p is scaled to give initial uniform diffusivity of 1×10^{-6} m^2/s.

SM5 and SM6. Denudation in fluvial landscapes is largely set by the efficiency of fluvial erosion, here modeled using a variation of the stream-power law. We chose typical values for the various coefficients of the extended stream-power law (Whipple & Tucker, 1999; Yuan et al., 2019), with $K_c = 1 \times 10^{-2} m^{-2}/yr$, $G = 1$, $m = 0.4$, $n = 1$. Fluvial erosion is strongly dependent on the fluvial erodibility K_f, which incorporates variations as a function of rock type, climate, vegetation, and erosive agents (Braun, 2006; Cowie et al., 2008; Stock & Montgomery, 1999). Given $m = 0.4$, $n = 1$, typical values of K_f lie between 1×10^{-6} $m^{0.2}/yr$ to 1×10^{-4} $m^{0.2}/yr$ (Stock & Montgomery, 1999). We test the effects of surface process efficiency on mountain growth with two end-member models with $K_f = 0.5 \times 10^{-5}$ $m^{0.2}/yr$ and $K_f = 5 \times 10^{-5}$ $m^{0.2}/yr$, respectively. For simplicity, deposited sediments have the same nominal density and rheological properties as upper crust. The relatively high sediment density slightly overestimates sedimentary loading, but is considered sufficient. Furthermore, we do not focus on the highly dynamic evolution of the landscape on top of the mountain belt, but rather investigate the large scale effects of surface processes on mountain belt formation.

2.2. Parameter Variations in the Models Presented

With a set of seven models (Table 2) we test the effects of depleted lithospheric mantle (M1, M2, M3), and thus slab pull, extensional inheritance (M4), surface process efficiency (M5, M6), and surface processes with a weak salt décollement (M7) on the evolution of an orogen from small and cold to large and hot. In models M1, M2, and M3 we monitor the pull exerted by the subducting lithospheric mantle and the tectonic boundary force in the lithosphere at the model boundaries (see Section A4). The latter give insight into the force balance required to drive mountain belt growth. Animations of each model and the Fastscape-model plots of M5 to M7 can be found in the supplementary material. The supplement also contains six additional

Table 2
Parameter Variations in the Models Presented

Model nr.	Model name	Test parameter	Parameter value	Explanation
M1	MRef	–	$\Delta\rho_{0,m} = 0$ kg m^{-3}	Shows influence of pulling slab; reference model
M2	M20kg	ρ_0 of lithospheric mantle	$\Delta\rho_{0,m} = 20$ kg m^{-3}	Shows influence of neutrally buoyant slab
M3	M40kg	ρ_0 of lithospheric mantle	$\Delta\rho_{0,m} = 40$ kg m^{-3}	Shows influence of positively buoyant slab
M4	MExt	Boundary condition	150 km extension before convergence	Shows influence of preorogenic extension
M5	MSpLow	Low surface process efficiency	$K_f = 0.5 \times 10^{-5}$ m$^{0.2}$/yr	Shows influence of low surface process efficiency
M6	MSpHigh	High surface process efficiency	$K_f = 5 \times 10^{-5}$ m$^{0.2}$/yr	Shows influence of high surface process efficiency
M7	MSpDéc	Low surface process efficiency + weak décollement	$K_f = 0.5 \times 10^{-5}$ m$^{0.2}$/yr, $\eta_{décollement} = 1 \times 10^{19}$ Pas	Shows influence of decoupling between thick and thin-skinned tectonics
Supplementary models				
SM1	SMleft	Velocity b.c. only on left side	$v_{left} = 1$ cm/yr, $v_{right} = 0$ cm/yr	Shows that model evolution is independent of absolute plate movement
SM2	SMright	Velocity b.c. only on right side	$v_{left} = 0$ cm/yr, $v_{right} = 1$ cm/yr	Shows that model evolution is independent of absolute plate movement
SM3	SMvel3	Convergence velocity	$v_{left} = v_{right} = 1.5$ cm/yr	Shows influence of high convergence velocity on plateau formation
SM4	SMhighH	Crustal radioactive heat production	$H_{UC,MC} = 1.63$ μW m^{-3}, $H_{LC} = 0$	Shows influence of high radioactive heat production in upper & middle crust
SM5	SMSpMed	Medium surface process efficiency	$K_f = 1 \times 10^{-5}$ m$^{0.2}$/yr	Shows influence of moderately high surface process efficiency
SM6	MSpVeryHigh	Very high surface process efficiency	$K_f = 7.5 \times 10^{-5}$ m$^{0.2}$/yr	Shows influence of very high surface process efficiency

Note. Models 2–6 are different from the reference model M1 in one parameter, model 7 is different from model 5 in one parameter. $\Delta\rho_{0,m}$ is the density difference between sublithospheric and lithospheric mantle at surface temperature.

models testing boundary condition kinematics, convergence velocity, crustal heat production, and medium respectively very high surface process efficiency (Table 2).

3. Results

3.1. Reference Model M1 (MRef): No Depletion of Lithospheric Mantle

Convergence initiates deformation at the weak seed, forming a triangular uplifted plug. Subsequent shortening produces thick-skinned thrust sheets on the pro-side, and the pro-side lithospheric mantle and lower crust start to subduct (Figure 2a). Subduction deflects the Moho isotherm downwards, leading to a cold and small orogen. Ongoing convergence results in more pro-side shortening, and formation of a first crustal retro-side thrust sheet. At the same time, the strong retro-lithosphere bends downwards and the orogen starts to (1) heat up and (2) migrate onto the retro-lithosphere (Figure 2b). Further orogenic shortening forms thrust sheets on the pro-and retro-sides, and the orogen translates onto the indenting retro-lower crust and mantle. Translation of pro-side thrust sheets onto the retro-side creates inclined to recumbent folds facing to the retro-wedge and flat lying foliation on top of the lower crust (Figure 2b, viscosity inset). Radioactive heating of thickened crustal material lowers the middle crustal viscosity and the retro-Moho starts to become horizontal after 500 km of convergence, when the viscously weak crust has reached a temperature of ~700°C. Onset of retro-Moho flattening coincides to first order with formation of a plateau on the retro-side (Figure 2c). Once deformation starts on the retro-wedge, i.e., after >150 km of convergence, shortening is distributed into 60% pro-wedge and 40% retro-wedge deformation; the pro-wedge grows in width by ~5 km/Myr and the retro-wedge by ~3.3 km/Myr.

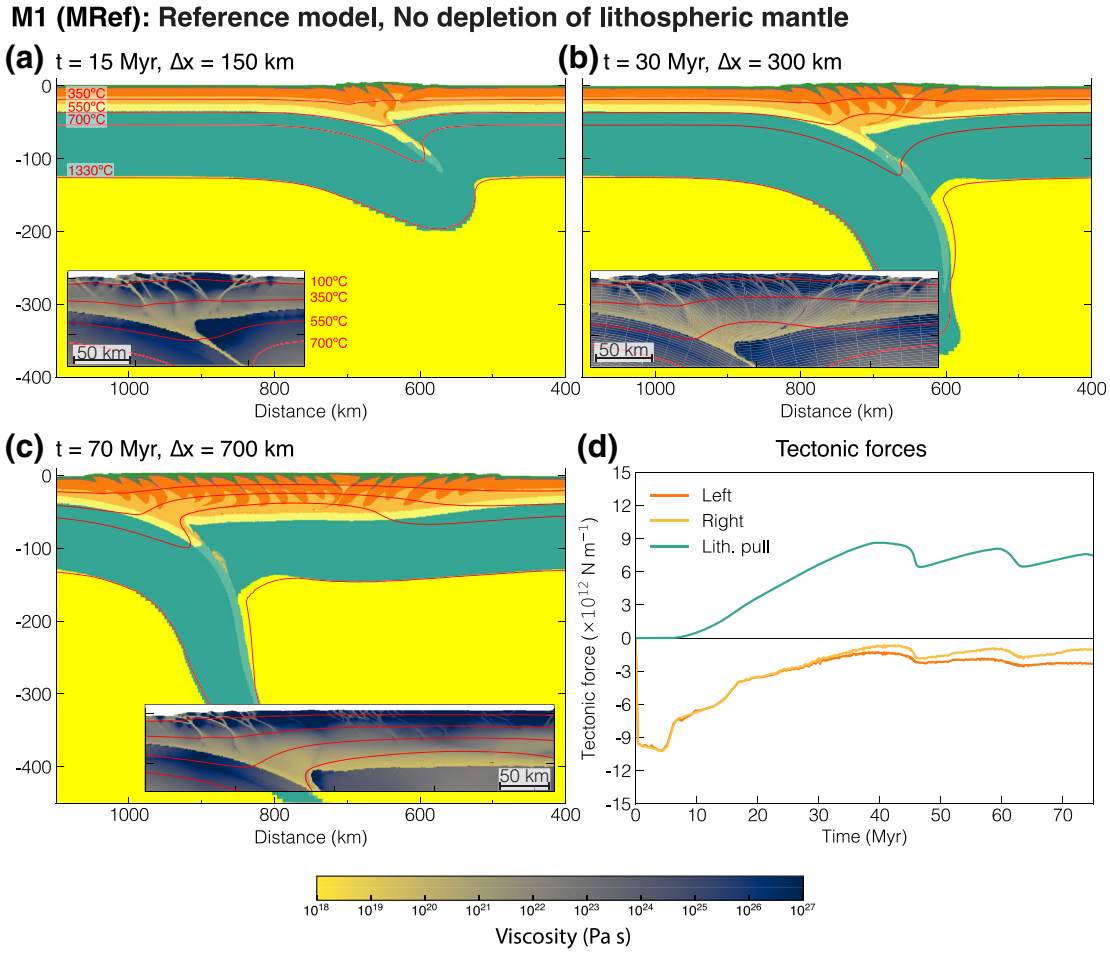

Figure 2. Reference model M1 (MRef) without depletion of the lithospheric mantle. (a, c) Material colors (see Figure 1) with isotherms. t is model time, Δx is the amount of convergence. The zoom insets show the viscosity field with logarithmic colormap and temperature isotherms. The viscosity inset in (b) also shows a gray grid passively tracking deformation. (d) Tectonic forces (integrated horizontal deviatoric stresses) at the left and right boundaries. Negative values are compressional. Additionally, the integrated pull (positive value is pull) exerted by the subducting lithospheric slab is shown as green line. See supplementary material for a model animation (MS01).

The model evolution is reflected in the evolution of the tectonic boundary forces (see Methods section for computation of forces). The pull exerted by the subducting lithospheric mantle increases up to 9×10^{12} N m^{-1}. Simultaneously, the compressional tectonic force at the left and right boundary decreases from 9×10^{12} N m^{-1} to $\sim 2 \times 10^{12}$ N m^{-1}. Two drops in lithospheric pull and tectonic forces after ~45 Myr and ~65 Myr are caused by two drips of the subducting lithospheric mantle (see supplementary video MS1). Supplementary models SM1 (MRef_right) and SM2 (MRef_left) with full velocity boundary conditions applied only on the right and left side, respectively, show that model evolution is independent of the direction of plate movement (supplementary Figure S1). A supplementary model with higher upper- and middle-crustal heat production (SM4, SMhighH) shows retro-Moho-flattening and thus plateau formation after less convergence and with a lower crustal thickness, and a supplementary model with high convergence velocity (SM3, SMvel3) shows plateau formation after greater amounts of convergence and with a thicker crust (supplementary Figure S2).

3.2. Models M2 and M3: Depleted Lithospheric Mantle

Models M2 (M20kg, Figures 3a and 3b) and M3 (M40kg, Figures 3c and 3d) with 20 and 40 kg m^{-3} nominal depletion, respectively, show a very similar crustal evolution as the reference model. Shortening initial-

ly creates thrust sheets only on the pro-side. After more than 150 km of convergence, retro-shortening starts, the orogen moves onto the retro-plate, and shortening is distributed into 60% pro-wedge and 40% retro-wedge deformation.

The influence of lithospheric depletion can be seen in the deep structure. In M2 the cold subducting lithosphere is initially negatively buoyant and subducts. Conductive heating leads to late upward bending of the subducting lithosphere (Figure 3a). The subducting lithospheric mantle exerts a small pull of maximum $\sim 3 \times 10^{12}$ N m^{-1} and the compressional tectonic forces at the side are on average at $\sim 4 \times 10^{12}$ N m^{-1} (Figure 3b). In M3 the downgoing lithospheric mantle and lower crust are always positively buoyant and thrust under the overlying mantle (Figure 3c). The buoyancy force exerted by the resulting lithospheric slab increases steadily up to $\sim 10 \times 10^{12}$ N m^{-1} and the compressional tectonic boundary forces are in the order of $\sim 6 \times 10^{12}$ N m^{-1}.

3.3. Model 4 (MExt): No Lithospheric Depletion, With Extensional Inheritance

Model M4 has the same setup as model M1, but convergence is preceded by 150 km of extension. Extension creates an asymmetric margin that is, almost fully broken up, with several extensional blocks on the right side and a narrow extensional domain on the left side (Figure 4a). Inversion of the passive margin re-activates the weak extensional structures and creates a structurally complex central plug. Inversion also traps small fragments of exhumed lithospheric and upper mantle in the uplifted plug (Figure 4b).

The subsequent model evolution is similar to the reference model, with creation of thrust sheets mainly on the pro-side, before onset of retro-side thrusting and migration of the mountain belt onto the retro side. The uplifted plug composed of weak extensional structures leads to earlier loading of the retro-side and simultaneously delays formation of thick-skinned thrust sheets on the retro-side (Figures 4c and 4d).

3.4. Model 5 (MSpLow): No Lithospheric Depletion, With Low Surface Process Efficiency

Model M5 (MSpLow) has the same setup as model M1 (MRef), and additionally includes surface processes with spatially and temporally uniform values (Figure 5, supplementary Figure S3 for corresponding Fastscape snapshots). Fluvial erodibility $K_f = 0.5 \times 10^{-5}$ m$^{0.2}$/yr, which leads to low surface process efficiency.

The crustal evolution is again similar to the reference model with initial thrusting on the pro-side, before retro-thrusting starts and the orogen migrates onto the overlying plate (Figure 5). Growing topography leads to increased erosion and sedimentation, which fills the evolving foreland basin. New thick-skinned thrusts progressively capture the filled foreland basins and transport them into the mountain belt, where the sediments get re-eroded. During the first 30 Myrs both evolving foreland basins are underfilled, while between 35 and 50 Myrs, foreland basin filling and capture by new thrusts occur roughly on the same timescale (Figure 6a). The recycling of sediments deposited in the foreland into the orogen leads to no net-loss of material by erosion during the first ~50 Myr. With ongoing orogenic growth, erosion outpaces deposition and orogenic crustal accretion is delayed by on average ~15%. Consequently, mountain width is similar to M1 during the first ~50 Myr, and slightly but consistently lower during the consecutive 25 Myrs (Figure 6c). The crustal thrust sheets become slightly wider with increasing sedimentation, most pronounced on the retro-side (Figures 5b and 5c). Some thin-skinned thrust sheets form in the foreland basins, detaching in the frictional décollement layer (Figures 5b and 5c). Erosion slowly exhumes the thrust sheets in the center of the mountain belt.

A supplementary model with medium fluvial erodibility $K_f = 1 \times 10^{-5}$ m$^{0.2}$/yr (see supplementary Figures S6 and S7) shows a similar evolution. However, already after ~30 Myr erosion is more effective than deposition, and the subsequent orogenic growth is delayed on average by 30%–40% (Figure 6c).

3.5. Model 6 (MSpHigh): No Lithospheric Depletion, With High Surface Process Efficiency

Model M6 (MSpHigh) has the same setup as M5 (MSpLow), but includes highly efficient surface processes with a fluvial erodibility $K_f = 5 \times 10^{-5}$ m$^{0.2}$/yr.

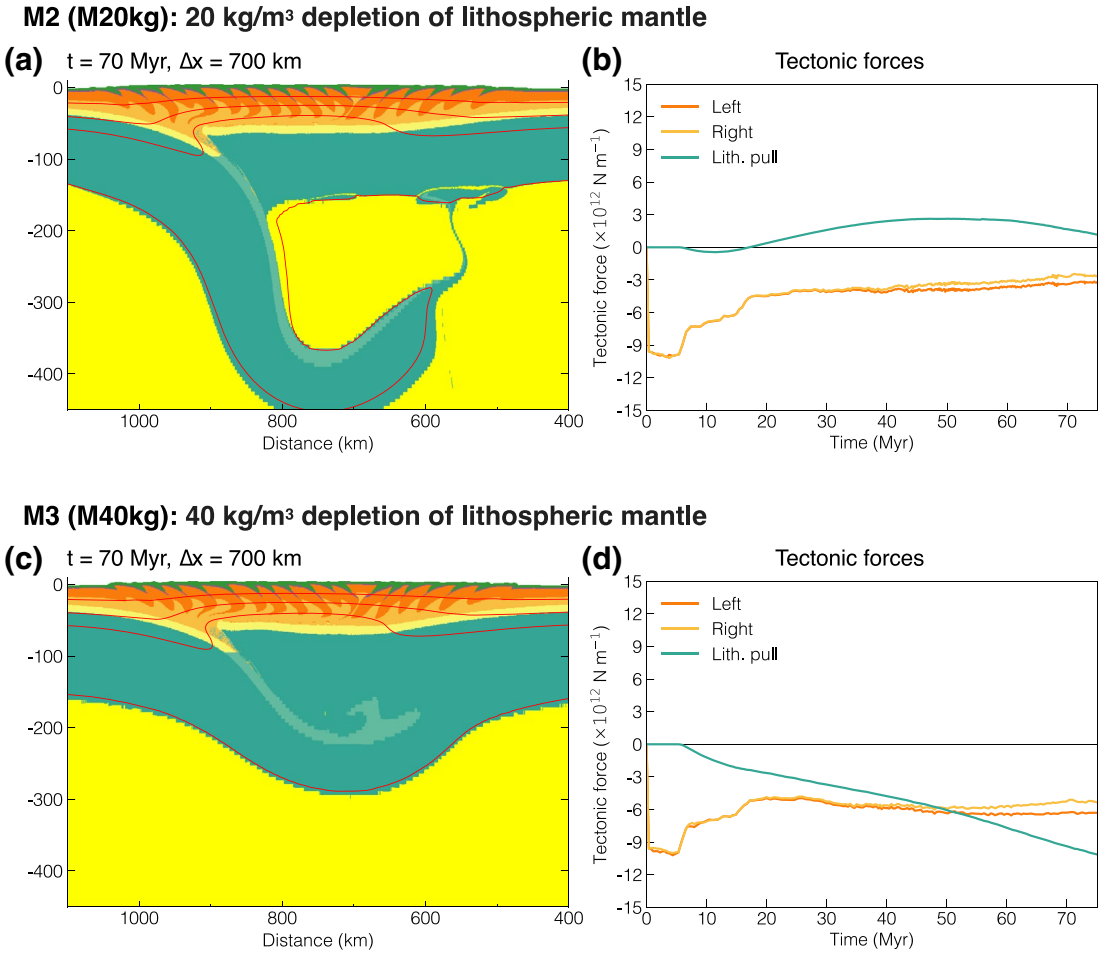

Figure 3. Models M2 (M20 kg, a and b) and M3 (M40 kg, c and d) with respectively 20 and 40 kg m^{-3} depletion of the lithospheric mantle. (a, c) Material colors (see Figure 1) with isotherms (350°C, 550°C, 700°C, and 1,330°C). t is model time, Δx is the amount of convergence. Snapshots are flipped left-right (see *x*-axis) to simplify comparison with the other models. (b and d) Tectonic forces (integrated horizontal deviatoric stresses) at the left and right boundaries. Negative values are compressional. The integrated pull exerted by the subducting lithospheric slab is shown as green line. Positive values represent overall pull and negative values overall push. See supplementary material for model animations (MS02, MS03).

Initial shortening creates an uplifted plug, and pro-side thrust sheets similar to the reference model. Erosion is very efficient already during the early stages of orogenic growth, leading to overfilled foreland basins, which are especially thick on the pro-side (Figure 7, Figure 6b). During the whole model evolution, thick-skinned thrusts only form on the pro-side apart from one retro-thrust sheet forming after ~20 Myr. Thrusts capture the filled foreland basins and form thick-skinned thrust sheets. Thrust sheets have a similar size as in the reference model (M1) during the first 15 Myr of model evolution, and are wider once they capture the thick, filled foreland basins (Figures 7a and 7b). Some decoupling between thin-and thick-skinned deformation can be observed, especially once the foreland basins are thick (Figures 7b and 7c). Efficient erosion exhumes the thrust sheets in the core of the mountain belt, which advects the temperature field and creates a high geothermal gradient at the surface. The life-span of thick-skinned thrust sheets between formation, transport into the orogen core and erosion is typically 20 Myr. Erosion almost balances crustal accretion so that the orogen only grows several 10s of km in width during the last 50 Myr of model evolution (Figures 6b and 6c). Throughout the model run, the retro-side lower crust and lithospheric mantle slowly thrust under the orogen and the mountain belt migrates onto the retro-side (Figure 7c).

Supplementary model SM6, with very high fluvial erodibility $K_f = 7.5 \times 10^{-5}$ $m^{0.2}$/yr shows that an even higher surface process efficiency leads to a steady state between erosion and tectonic accretion (supplementary Figure S8 and S9, Figure 7c). Crustal evolution in the supplementary model is similar to M6 (MSpHigh),

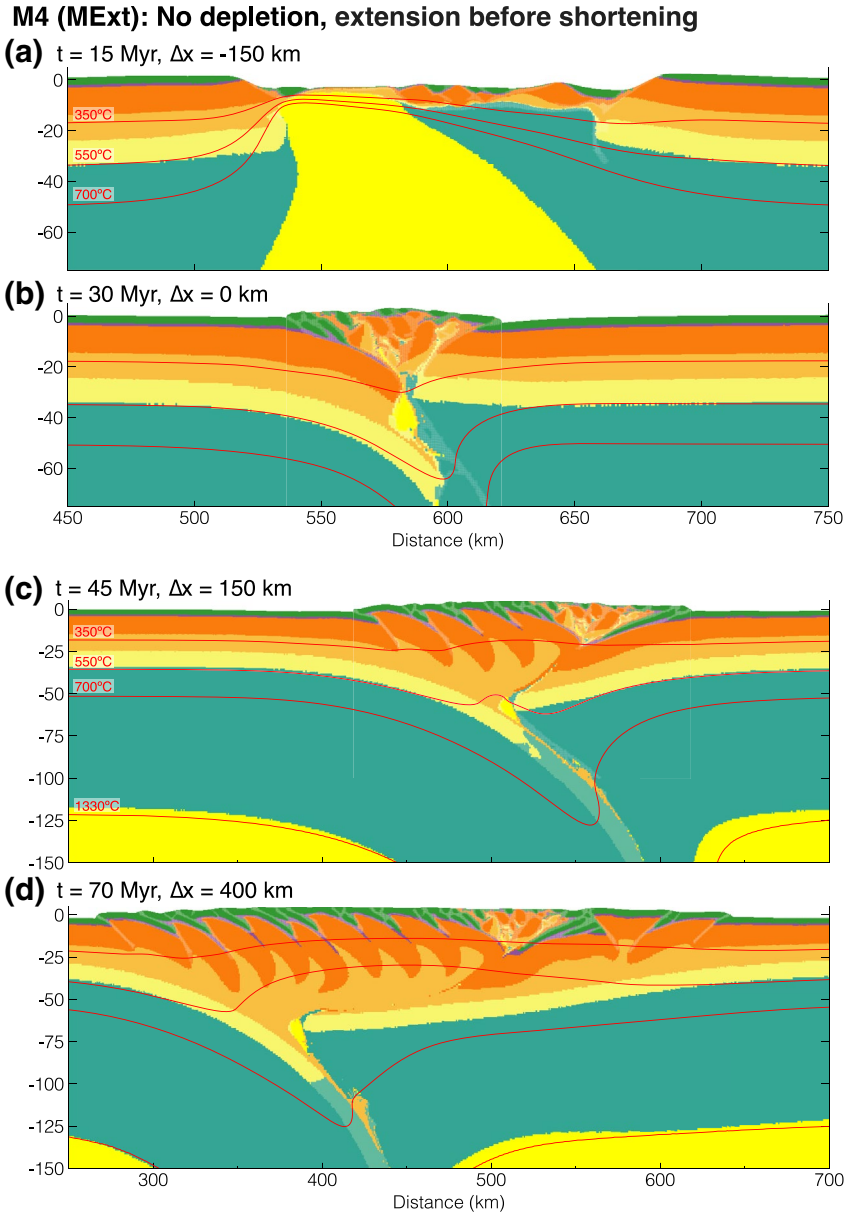

Figure 4. Model M4 (MExt) without depletion of the lithospheric mantle but with 150 km of extensional inheritance. (a–d) Material colors (see Figure 1) with isotherms. t is model time, Δx is the amount of convergence. The white, transparent overlay highlights strain-weakened shear zones.

with thrust sheets forming primarily on the retro-side, thick foreland basins, and slow underthrusting of the lower retro-lithosphere.

3.6. Model 7 (MSpDéc): No Lithospheric Depletion, With Surface Processes, With Weak Salt Décollement

Model M7 (MSpDéc) has the same setup as model M5 with low surface process efficiency, but a much weaker décollement horizon with constant viscosity of 1×10^{19} Pa s (Figure 8, supplementary Figure S5 for corresponding Fastscape snapshots). The model is 500 km wider than the others to prevent interaction of the evolving foreland fold-thrust belt with the side boundaries. The numerical resolution is kept constant by increasing the amount of finite elements.

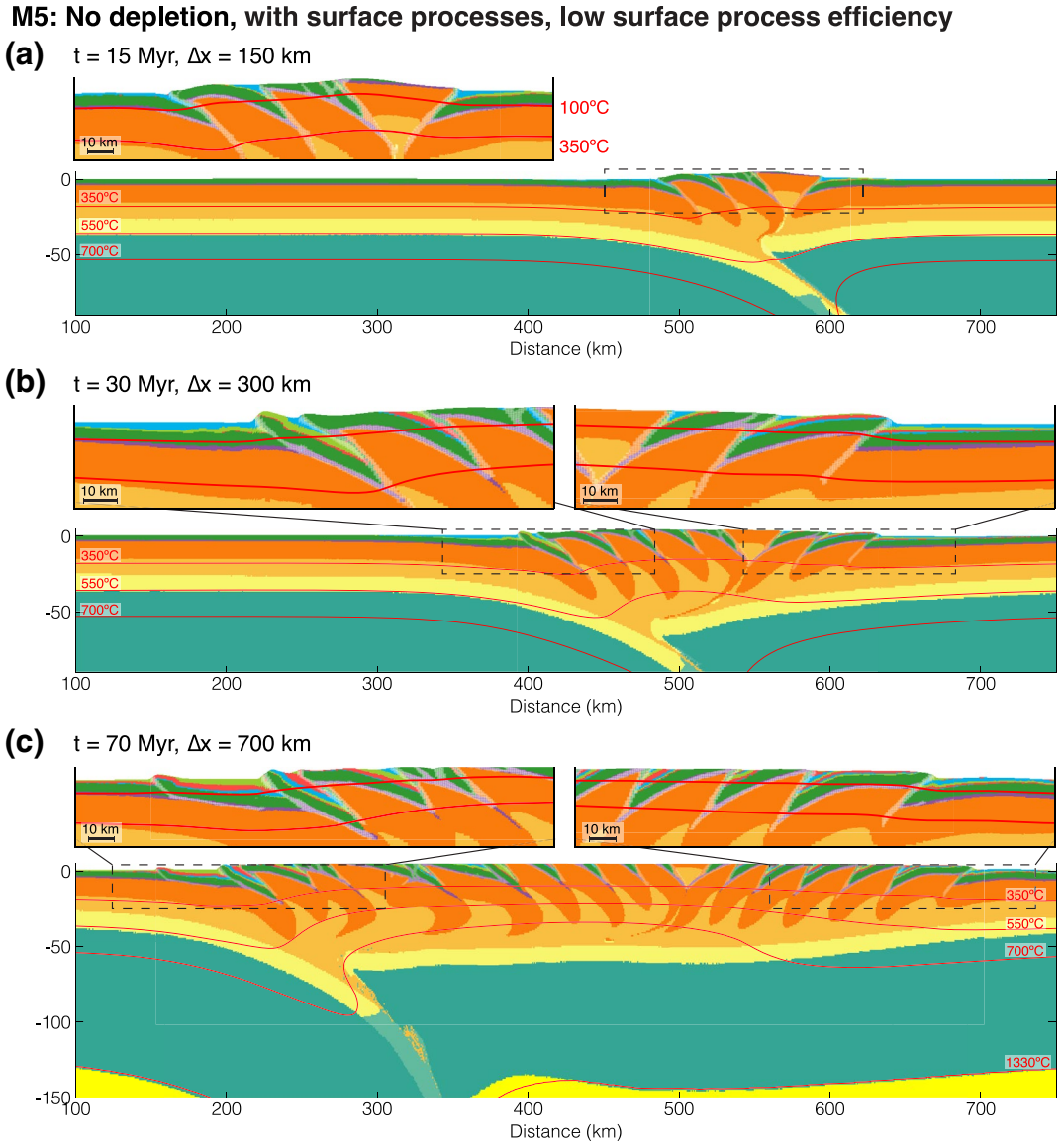

Figure 5. Model M5 (MSpLow) without depletion of the lithospheric mantle, including a full coupling with surface processes. Surface process efficiency is medium, with $K_f = 0.5 \times 10^{-5}$ $m^{0.2}$/yr. (a–c) Material colors (see Figure 1) with isotherms. t is model time, Δx is the amount of convergence. Zoom insets show close-up of crustal domains. The white, transparent overlay highlights strain-weakened shear zones. Note the small thin-skinned foreland fold-thrust belt on pro- (and retro-) side, detaching in the décollement horizon (purple). Corresponding Fastscape surfaces can be found in supplementary Figure S3.

The large-scale crustal evolution is again similar to the reference model with initial thrusting on the pro-side, before retro-thrusting starts and the orogen migrates onto the overlying plate. The weak décollement effectively decouples the thick-and thin-skinned deformation in the mountain belt and thin-skinned foreland fold-thrust belts develop in both foreland basins. During the first 150 km of convergence, the syn-deformation sediment supply is limited and many small thin-skinned thrust sheets form on the pro-side and in the center of the orogen (Figure 8a). With increased shortening, the topography grows and the sediment supply increases. Large and long thin-skinned thrust sheets form on the pro-side and also the retro-foreland basin deforms. The thick-skinned thrust sheets in the center of the orogen have a shallower dip than those in models 1–6 (Figure 8b). With further shortening the pro-side foreland fold-thrust belt forms new thrust sheets, shortens internally, and becomes thicker. Newly forming thick-skinned thrusts do not break the

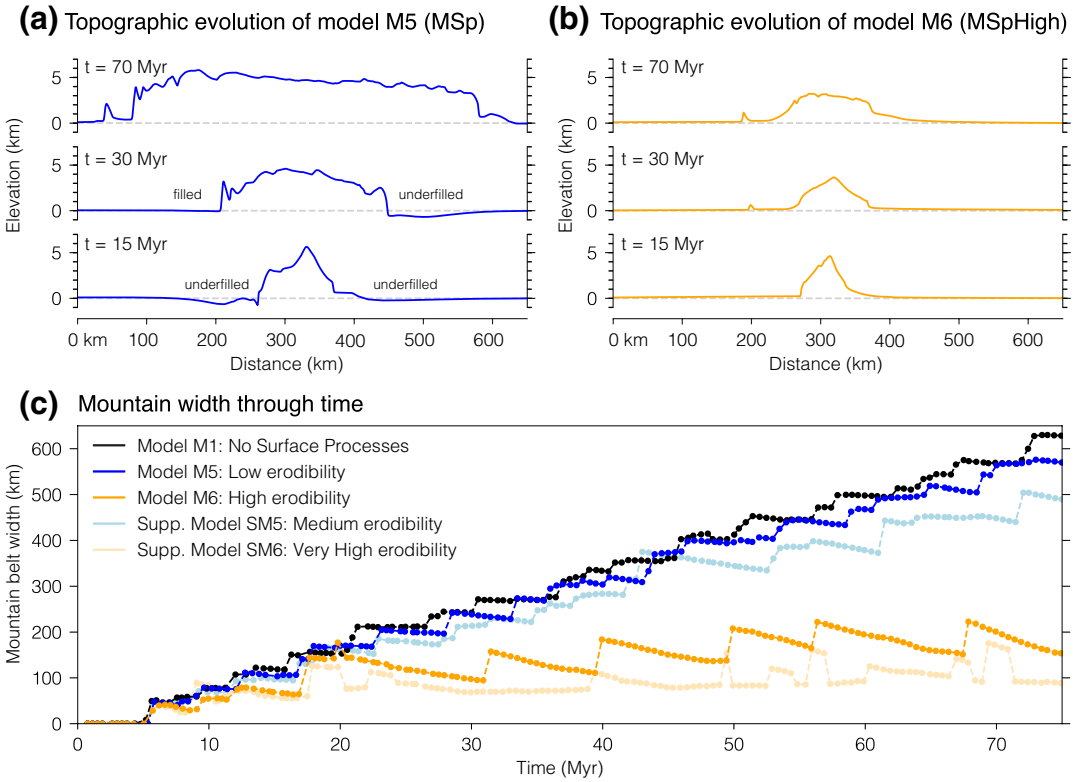

Figure 6. (a and b) Topographic evolution of models MSpLow and MSpHigh. (c) Plot of mountain width through time. The mountain width is calculated every 0.5 Myrs between the two outermost points which are above 1,000 m. Steps in width correspond to new outward-propagating thrusts.

foreland belt, but come up in the back of the foreland belt and form an antiformal duplex stack (Figure 8c). The retro-side foreland fold-thrust belt records less shortening than the pro-side.

4. Discussion

We present a suite of geodynamic numerical models that investigate the influence of slab pull, extensional inheritance, surface processes, and a weak décollement horizon on mountain-belt growth from small and cold to large and hot. In the following sections we will first discuss the influence of each of these tested factors on the distribution of deformation and structural style during growth. Subsequently, we derive a simple force-balance analysis, which quantifies thrust formation and the interaction between thin-and thick-skinned deformation, followed by a section addressing model limitations and a comparison to previous modeling studies.

4.1. Distribution of Shortening as a Function of Orogen Size

All models shown here exhibit a similar distribution of crustal shortening that develops as a function of orogen size (Figure 9). In models without surface processes, orogen size is a function of plate convergence. Since erosion counteracts orogenic growth, different stages of orogen evolution are most accurately described as a function of cross-sectional area (CA = plate convergence times crustal decoupling depth minus erosion):

If the orogen is small and cold, continent-continent collision creates a structurally mono-vergent wedge consisting of the uplifted plug (U) and several pro-side thrust sheets (P). The retro-lithosphere acts as an indenter and does not form thrust sheets (Figure 9b). The cross-sectional area is lower than 3.75×10^9 m^2, corresponding to at most 150 km of convergence in M1. Increased shortening leads to loading of the retro-plate, heating of the orogen, and retro-wedge (R) deformation, forming a transitional orogen defined by a structurally bi-vergent wedge (Figure 9c). With ongoing convergence, the strong retro-lithosphere thrusts

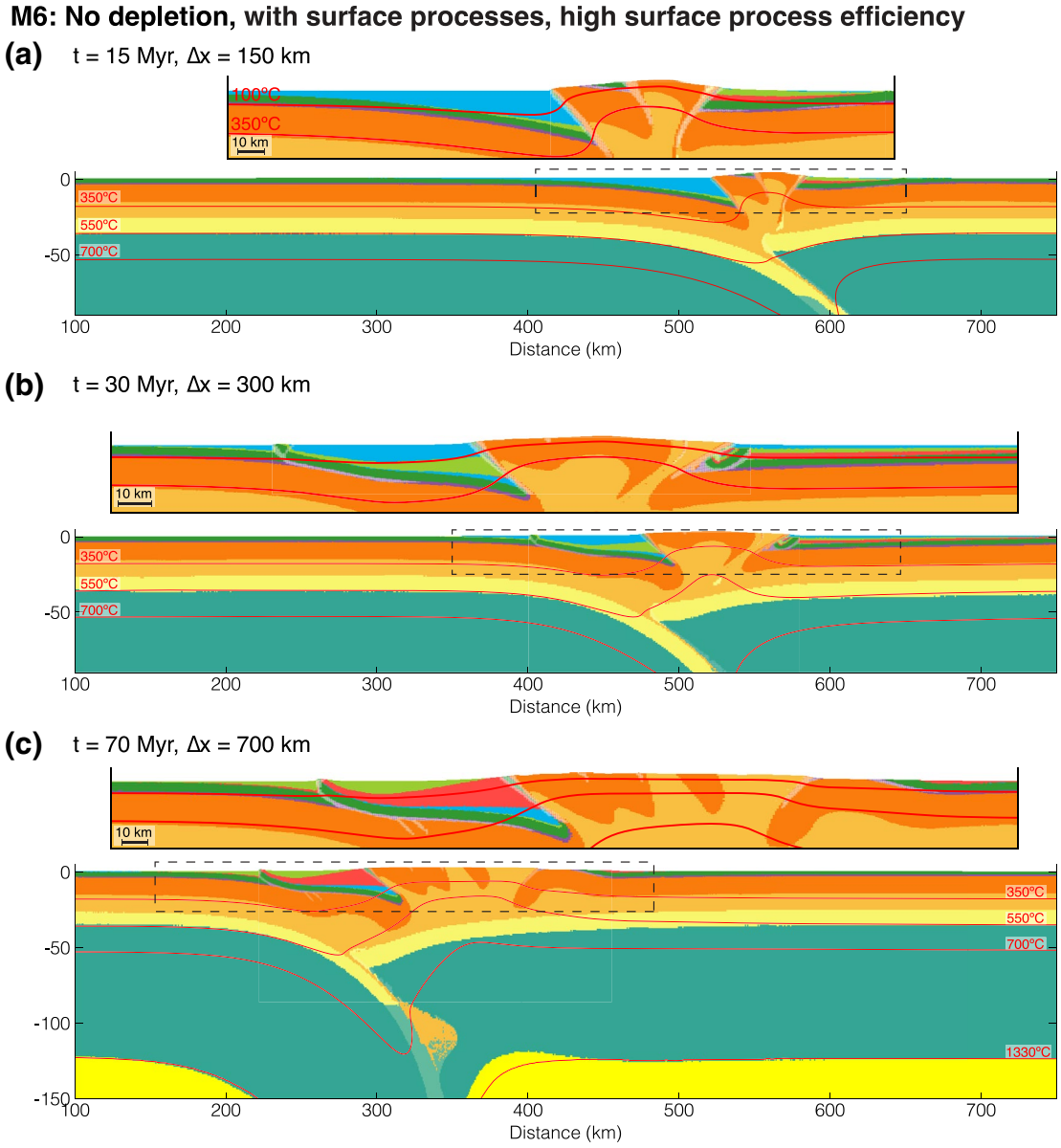

Figure 7. Model M6 (MSpHigh) without depletion of the lithospheric mantle, including a full coupling with surface processes. Surface process efficiency is high, with $K_f = 5 \times 10^{-5}$ m$^{0.2}$/yr. (a–c) Material colors (see Figure 1) with isotherms. t is model time, Δx is the amount of convergence. Zoom insets show close-up of crustal domains. The white, transparent overlay highlights strain-weakened shear zones. Note the thin-skinned foreland fold-thrust belt on pro- (and retro-) side, detaching in the décollement horizon (purple). Corresponding Fastscape surfaces can be found in supplementary Figure S4.

under the pro-wedge, which results in tight, overturned folds with flat-lying foliation on top of the lower crust (Figure 9d). A central, elevated plateau with a flat Moho, characteristic for a large, hot orogen, forms once CA > 12.5×10^9 m^2, equivalent to >500 km of convergence in reference model M1. Underthrusting of the retro-side lithosphere and steady evolution of crustal shortening and thickening highlights the decoupled evolution of crust and mantle in large and hot orogens. Convergence is partitioned to 60% pro- and 40% retro-side deformation after onset of retro-wedge shortening (Δx > 150 km in M1). Supplementary Figure S10 shows the distribution of shortening as a function of convergence in M1.

We identify several aspects that naturally develop in our models and are needed for the characteristic evolution presented above (Figure 9a): A pro-and retro-step-up shear zone (Willett et al., 1993), a mantle singularity (S-point), and a viscous decoupling horizon in the crust. All of those aspects can be inferred in

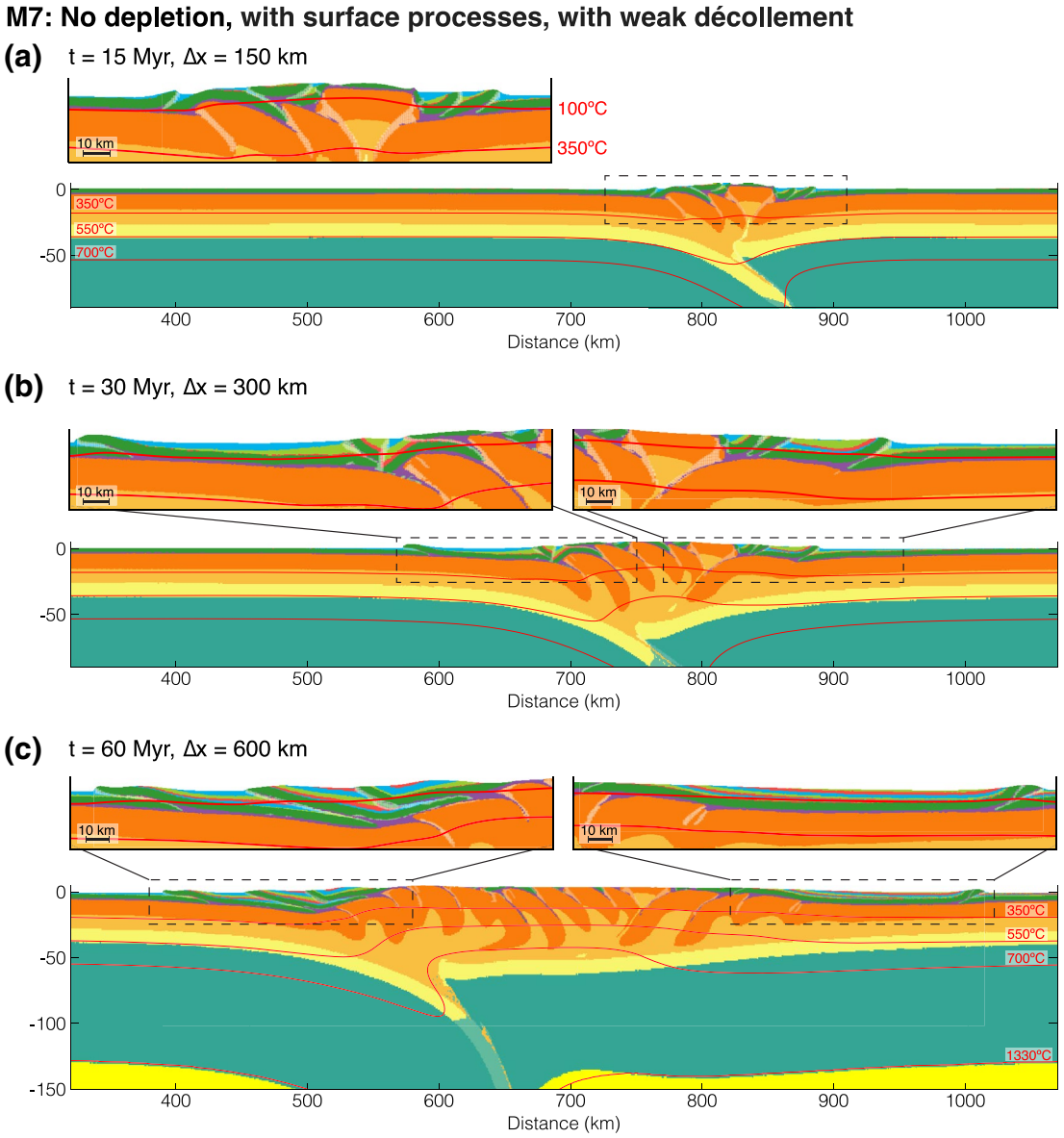

Figure 8. Model M7 (MSpDéc) without depletion of the lithospheric mantle, including a full coupling with surface processes and with a weak salt décollement with fixed viscosity of 1×10^{19} Pa s. (a–c) Material colors (see Figure 1) with isotherms. t is model time, Δx is the amount of convergence. Zoom insets show close-up of crustal domains. The white, transparent overlay highlights strain-weakened shear zones. Note the thin-skinned foreland fold-thrust belts on pro- and retro-side, detaching in the very weak décollement horizon (purple). Corresponding Fastscape surfaces can be found in supplementary Figure S5.

the Pyrenees, Alps, and Himalayas, and we will compare the shortening distribution and other features with those orogens below. However, as will become apparent in the comparison to the Himalayan-Tibetan orogen, if any of the four primary controlling factors is altered in a mountain belt on Earth, the orogen will develop differently, which in turn gives important insight into the peculiarities of this mountain belt. The importance and existence of the retro-step-up shear zone is discussed below.

We define the onset of plateau formation with flattening of the retro-side Moho. A horizontal Moho implies that the radioactively heated, weak viscous base of the upper crust does not support and flows laterally under applied pressure gradients. The onset of plateau formation is dependent on viscous weakening resulting from crustal thickening and associated radioactive heating, and has a thermal equilibration timescale independent of convergence rate. The difference between convergence rate and the timescale of thermal equilibration explains delayed plateau formation in the supplementary model with high convergence velocity

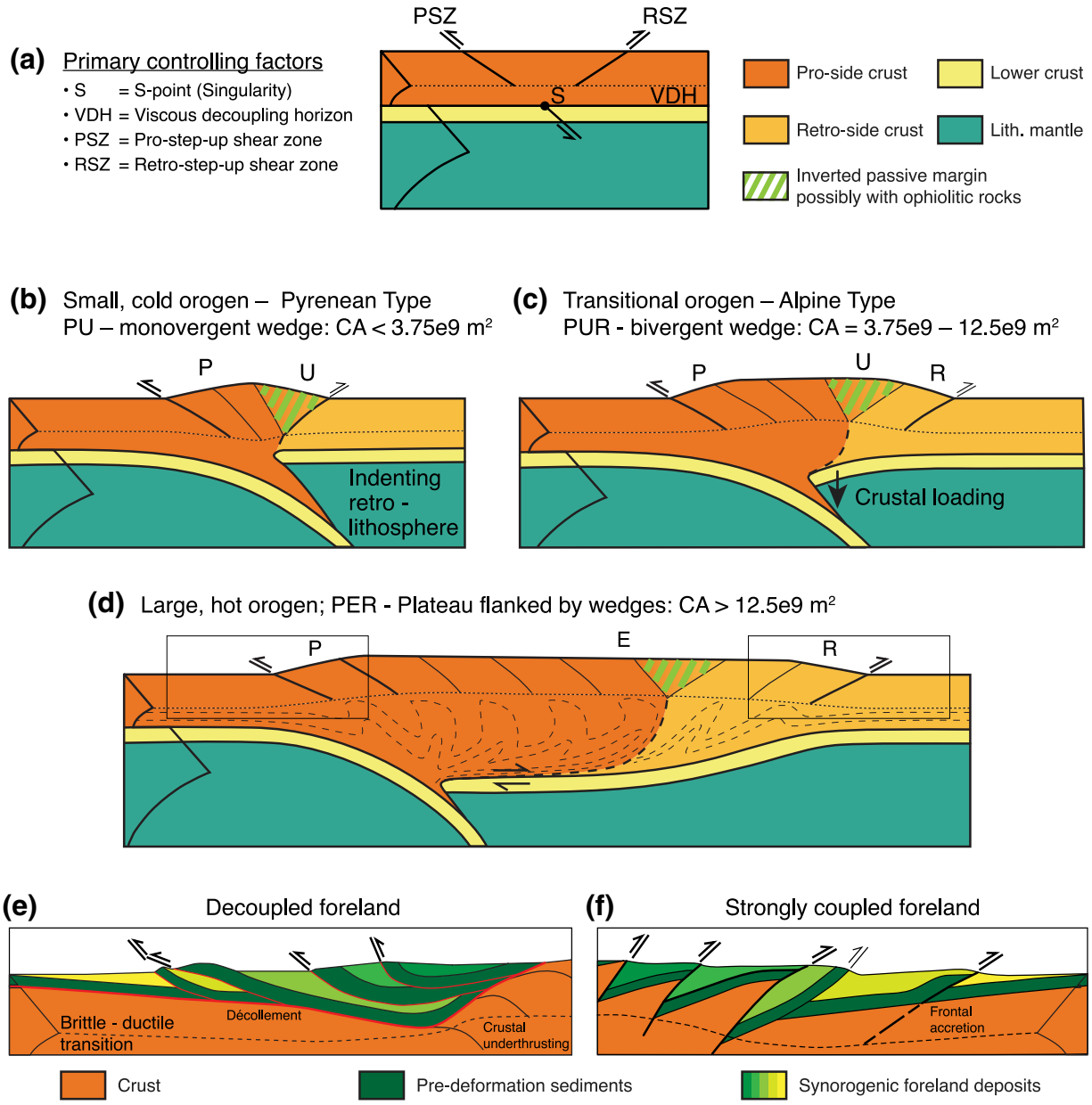

Figure 9. Distribution of shortening during mountain building from small and cold to large and hot. (a) Given the existence of a viscous decoupling horizon in the mid or lower crust and a pro- and retro-side thrust and mantle singularity, a mountain belt is expected to develop in the following manner: (b) Initial inversion of inherited structures forms an uplifted plug (U) and deformation on the pro-side (P). The retro-side is acting as indenter. (c) Ongoing shortening loads the retro-plate and the retro-side shortens (R). The retro-side lithosphere starts to thrust under the central part of the orogen, which creates tight, inclined to recumbent folds with flat-lying foliation on top of the lower crust. It is worth noting that the vergence of these deep folds is the opposite with respect to the upper crustal ones (d). Further shortening is distributed into 60% on the pro-side and 40% on the retro-side. Ongoing horizontal shortening and crustal radioactive heating creates an orogenic plateau with a flat Moho (E). (e, f) Show the differences in structural style related to (de-)coupling of thin-and thick-skinned deformation.

(SMvel3). This model furthermore highlights that the convergence and cross-sectional area values for onset of plateau formation given above are a rough guideline and not unique for plateau formation on Earth.

4.1.1. The Influence of Lithospheric Depletion

Models M1 to M3 show the influence of depletion-related lithospheric density changes and thus pull of the subducting lower lithosphere on mountain-belt growth. The three models have a similar crustal evolution

in common despite a negatively (M1) or positively (M3) buoyant lithospheric mantle, which shows that orogenic growth and in particular the onset of retro-side shortening are largely independent of the negative or positive buoyancy of the subducting lower lithosphere, and solely a function of internal crustal loading. However, high lithospheric pull leads to low absolute tectonic boundary forces at the model sides, in the order of or less than ridge push ($\sim 3 \times 10^{12}$N m^{-1}, Turcotte & Schubert, 1982). The low tectonic forces show that in nature orogeny can occur at relatively low plate-driving forces, in the order of ridge push, in case of an undepleted lithospheric mantle or an oceanic slab that is, still attached to the subducting continental lithosphere. In contrast, orogenesis involving a refractory depleted mantle lithosphere requires significantly higher plate driving forces exceeding ridge push.

4.1.2. The Effects of Extensional Inheritance

Extension creates structural weaknesses that are reactivated during the inversion phase and form the central, uplifted plug. Inversion can incorporate mantle materials, exhumed to shallow depth during rifting, into the uplifted plug. Passive-margin inversion can be more complicated than shown in the models presented here, with large mantle blocks remaining in the upper crust as for instance seen in the Alpine Ivrea zone and possibly in the Pyrenean Labourd anomaly.

The idea that passive margins are the locus of deformation during continent-continent collision has long been proposed and is a fundamental part of the Wilson cycle (Wilson, 1966). Furthermore, it has been shown since the 1980s that the structural style and locus of deformation in many mountain belts, among others the Pyrenees, Alps, Andes, and Himalayan-Tibetan orogen are controlled by inherited rifts that predate shortening but become inverted and part of the orogen, as modeled in M4 (MExt, Amilibia et al., 2008; Beaumont et al., 2001; Carrera et al., 2006; Cooper & Williams, 1989; Gillcrist et al., 1987; Grier et al., 1991; Iaffa et al., 2011; Kapp & DeCelles, 2019; Muñoz, 1992). These observations corroborate model inferences that rifts will be the locus of deformation once boundary conditions change and show that the monotonous structural style of thick-skinned thrusts in our models is not expected to be equally observed in nature. Rather, preexisting extensional structures or any form of inherited weaknesses (e.g., R. W. H. Butler et al., 2006; Carrera & Muñoz, 2013) may control the position of new outward propagating thrusts.

Above we showed a characteristic shortening distribution as a function of orogenic growth and explain that it requires a pro-and retro-step-up shear zone. Given that orogens on Earth typically have an initial phase of reactivation of inherited extensional faults or other types of weaknesses, it is also expected that orogens form both a pro- and a retro-step-up shear zone, thus potentially following the evolution of growth shown above. Removing the retro-shear zone has a profound effect on mountain-belt growth, as it does not allow retro-wedge loading and thus propagation of deformation onto the retro-wedge. This behavior is commonly observed in thermo-mechanical models that start with an inclined weak seed (Liao & Gerya, 2017), or subduction before collision (J. P. Butler et al., 2011), when weak inherited structures are not included in the model setup.

4.1.3. The Effects of Surface Processes

We tested the effects of surface processes on the evolution of orogen growth from small to large with two end-member models with respectively low and high surface-process efficiency. Erosion leads to exhumation of the central part of the orogen. Deposition of sediments in the foreland basin, subsequent recycling by thick-skinned thrusting and re-erosion in the core of the orogen buffers the effect of erosion. Once foreland basin filling is faster than creation of accommodation space through tectonics, i.e. once sediments bypass the foreland basin, orogenic growth will be slowed down. With low surface process efficiency, this transition occurs once the orogen has accumulated a cross-sectional area equivalent to 300–500 km of horizontal convergence in our models. If surface-process efficiency is high, the transition is reached once the initial uplifted plug has created significant topography, within few Myrs after the onset of shortening. High surface-process efficiency can create a steady state between tectonic material influx and erosional outflux. At (near-)steady state, the orogen remains in its growth phase (e.g., Figure 9), i.e., in case it is small, as in M6 (MSpHigh), it will keep producing thrust sheets mainly from the pro-side. Near-steady state during growth is characterized by strong metamorphic gradients of rocks exhumed to the surface and a high geothermal gradient at the surface. In contrast, orogenic growth far from steady state is characterized by little exhu-

mation in the core of the mountain belt, with possible preservation of syn- or preorogenic sedimentary deposits.

High erosion rates in the core of the mountain belt are reflected in thick foreland basin fill, most pronounced on the pro-side, which induces longer upper-crustal thrust sheets. This behavior can be best seen in the supplementary model with medium fluvial erodibility, leading to high sedimentation rates once the orogen is large and hot (supplementary Figures S6 and S7). The impact of deposition and erosion on the structural style of a mountain belt is further discussed in the force-balance section below.

The efficiency of surface processes should be assessed relative to the rate of surface uplift U (Equation A6), which in turn depends on the plate convergence rate. Therefore, the K_f values that we classify as leading to "low" or "high" surface process efficiency only apply if the convergence rate is 1 cm/yr, as used in our models. Lower convergence rates will have a similar effect as higher K_f, and vice versa.

4.1.4. The Influence of a Weak, Shallow Décollement

A weak décollement creates efficient decoupling between thick-skinned and thin-skinned structures. Furthermore, the combination of décollement strength and amount of syn-tectonic sediment determines the length of thin-skinned thrust sheets (Erdős et al., 2015; Fillon et al., 2013; Stockmal et al., 2007). Work-minimization favors long thrust sheets in case of abundant syn-tectonic sediments and a weak décollement, and vice versa (see Section below). The evolving thin-skinned foreland fold-thrust belt also has a feedback on thick-skinned tectonics. A large thin-skinned belt detaching in a weak layer, as seen in M6 (Figure 8c), is not incorporated by new thick-skinned thrust sheets. Rather, it slides forward during shortening and new thick-skinned thrusts come up in the hinterland, forming an antiformal duplex stack and leading to exhumation of basement rocks. Hence, a weak décollement horizon in combination with syn-tectonic sediments has a strong structural feedback on the mountain belt (Figure 9e), but does not alter the general distribution of shortening.

4.2. Dynamic Analysis of Thick- and Thin-Skinned Thrust Formation

We next quantify thrust formation during orogenic widening and the resulting variable structural styles using simple force-balance considerations. Orogenic growth is often explained using critical-wedge theory (Dahlen, 1984; Davis et al., 1983). However, critical-wedge theory does not account for viscous deformation, localized shear and strain-weakening of thrusts, and is hence not well suited to understand the dynamic evolution of deformation observed in our models. The dynamic analysis of thrust formation requires quantifying three types of forces: (a) the integrated strength, F_{int} required to deform parts of the lithospheric column, (b) the integrated viscous resistance of horizontal shear in different domains of the crust, F_V, and (c) the buoyancy force related to the topographic potential of the orogen, F_B. First, we will derive the typical reference thrust spacing (L_{Ref}) in our models, then investigate modifications to the reference thrust spacing and structural style as a function of inherited weaknesses, sedimentation and foreland decoupling (Figure 10).

Surface uplift through crustal thickening raises the topographic potential energy, which results in a horizontal force per meter orogen (F_B) that the mountain belt exerts onto its foreland. If this force equals the integrated strength F_{int} and overpressure P_o of the foreland, where $F_{\text{int}} \approx P_o$, i.e., if outward growth is energetically more favorable than continued surface uplift, a new outward propagating thrust forms and the orogen grows in width (Figure 10a, Molnar & Lyon-Caen, 1988; Sandiford & Powell, 1990; Schmalholz et al., 2014; Zhou & Sandiford, 1992). More specifically, and assuming efficient decoupling between crust and mantle lithosphere, outward propagating thrusting requires deformation of the unweakened upper-and middle crust (F_{int}) and viscous shear in the middle crust (F_V), which is balanced with F_B and continued slip on a strain-weakened shear zone in the orogen with strength F_{intWeak} (Figure 10a):

$$F_{int} + F_V = F_{intWeak} + 0.5 * F_B. \quad (1)$$

F_{int} of pristine model-crust is approximately 1.7×10^{12} N m^{-1} and strain-weakened crust has an integrated strength F_{intWeak} of $\sim 0.4 \times 10^{12}$ N m^{-1}, given a typical strain-rate $\dot{\epsilon} = 1 \times 10^{-14}$ s^{-1}. As discussed above,

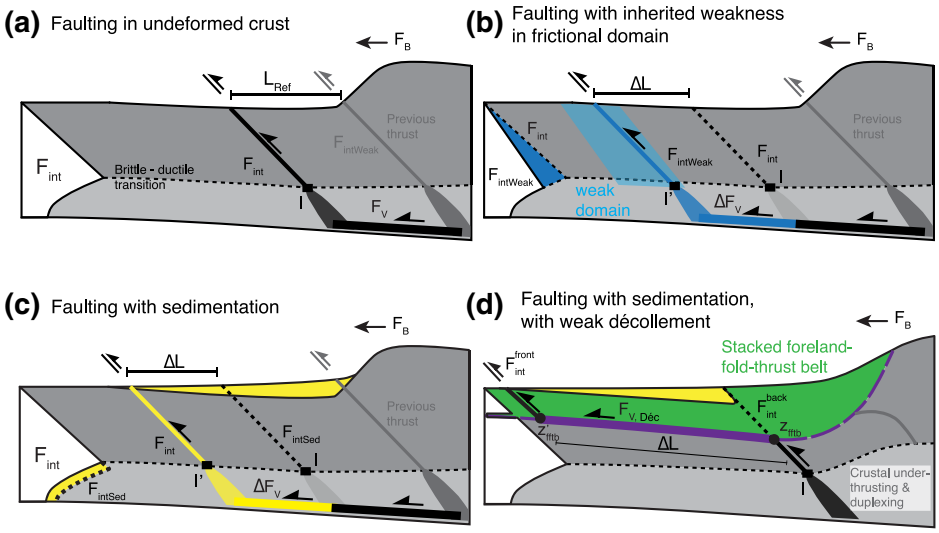

Figure 10. Theoretical cross sections through a mountain front with force considerations for different scenarios of lateral orogenic growth. Once the buoyancy force related to crustal thickening (F_B) exceeds the integrated strength of the crust (F_{int}), i.e., once outward growth is energetically more favorable than an increase in elevation, a new outward propagating thrust forms. (a) In the theoretical case of a homogeneous crust, new thrusts originate in *I* with constant thrust spacing of L_{Ref}. (b) Weak inherited structures will be re-activated if favored by the net force balance, increasing the potential thrust spacing by ΔL and possibly influencing the structural style of the mountain belt. (c) Sedimentation fills the evolving foreland basin and leads to strengthening of the crust if sedimentation rates are high. This leads to longer thick-skinned thrust sheets, as work minimization favors deformation of the crust further out in the basin. (d) If the crust contains a décollement layer (purple), the foreland fold-thrust belt can become decoupled from the thick-skinned deformation of the crust. Decoupling is favored if the décollement is weak and if the foreland-fold-thrust belt is thick through internal stacking or sediment loading.

$0.5{*}F_B$ is roughly equal to F_{int} (Molnar & Lyon-Caen, 1988; Schmalholz et al., 2014). $F_V = L_{Ref}\,2\eta\dot{\epsilon}$, where L_{Ref} is the reference thrust spacing and η middle crustal viscosity. Taking typical model values of $\eta = 1 \times 10^{21} - 2 \times 10^{21}$ Pa s, $\dot{\epsilon} = 2 \times 10^{-15} - 1 \times 10^{-14}\,\text{s}^{-1}$ gives $L_{\text{Ref}} = 10$ to 100 km. Our models without surface processes develop a steady, homogeneous pattern of thick-skinned thrust sheets with a horizontal thrust spacing L_{Ref} of 30–50 km (Figures 2–4), which fits well with our simple predictions (Figure 10a). In the following three paragraphs we will investigate how inherited weaknesses, sedimentation, and a weak décollement horizon modify L_{Ref} and influence the structural style of orogenic growth.

Assuming force balance, localization in a weak domain at location *I'* is favored over localization at the reference location *I* (Figure 10b) if:

$$F_{intWeak} + \Delta F_V \leq F_{int}, \tag{2}$$

where F_{int} and F_{intWeak} are the integrated strengths at *I* and *I'*, respectively, and ΔF_V is the force required to shear the viscous domain between *I* and *I'*. Given that $\Delta F_V = \Delta L 2\eta\dot{\epsilon}$, using typical model values (Figure 2), $\dot{\epsilon} = 1 \times 10^{-14}\,\text{s}^{-1}$, $\eta = 2 \times 10^{21}$ Pa s, and assuming a frictionally weak domain (Figure 10b) with strength equal to fully strain-weakened crust, results in a maximum thrust length increase $\Delta L = 32.5$ km. ΔL and L_{Ref} are therefore approximately equally large.

A similar relationship holds for the effect of sedimentation, as derived by Erdős et al. (2015). Sedimentation increases the strength of the crustal column above *I* and it is favorable to increase thrust sheet length (Figure 10c), if

$$F_{int} + \Delta F_V \leq F_{intSed}. \tag{3}$$

Using the same values for viscosity and strain rate as used above, $\Delta L = 20$ km for 5 km of syn-deformational sediments (Erdős et al., 2015), shows that the effect of sedimentation is potentially equally important as

the effect of inherited weaknesses. However, the calculation does not account for conductive and radioactive heating during deposition, which explains why thrust sheet lengthening is less pronounced in model MSpLow than in SMSpMed. Thrust sheet lengthening as a function of foreland basin fill relies on the supply of sediment, which increases with surface process efficiency and mountain belt size.

We show in model MSpDéc that a weak décollement horizon together with syntectonic sedimentation has a strong structural feedback on orogen style (Figures 9e and 9f). This can be readily understood by looking at the force balance of thrust formation with a weak décollement horizon (Figure 10d). In this case, thick-skinned thrusts will originate at the reference location I, creating a shear zone between I and the décollement horizon at z_{fftb}. Furthermore, if

$$F_{int}^{front} + F_{V,Déc} \leq F_{int}^{back}, \tag{4}$$

faulting will localize in the décollement horizon and the frontal thrust shown in (Figure 10d). Here, F_{int}^{front} and F_{int}^{back} are the integrated strengths of the frictional domain between the surface and the décollement at depth $z_{\mathrm{fftb}}^{'}$ and z_{fftb}, respectively, and $F_{V,Déc}$ is the force required to shear the décollement, which can thus also be expressed as:

$$\int_{surface}^{z_{fftb}^{'}} \left(P \cdot \sin(\phi_{eff}) + C \cdot \cos(\phi_{eff})\right) dz + \Delta L 2\eta\dot{\epsilon} \leq \int_{surface}^{z_{fftb}} \left(P \cdot \sin(\phi_{eff}) + C \cdot \cos(\phi_{eff})\right) dz. \tag{5}$$

Assuming lithostatic pressure, a negligible slope in the foreland fold-thrust belt, and a linear viscous décollement we can compute maximum ΔL analytically from Equation 5, with:

$$\Delta L \leq \frac{\left(0.5\rho g z^2 \sin(\phi_{eff}) + Cz\cos(\phi_{eff})\right)\Big|_{z_{fftb}}^{z_{fftb}^{'}}}{2\eta\dot{\epsilon}}, \tag{6}$$

see Methods section and Table 1 for parameter definitions and values. Assuming values motivated from model MSpDéc, thin-skinned thrusting would capture a 1 km thick sedimentary wedge of up to $\Delta L = 223$ km length. If the wedge is smaller, the thin-skinned fault will localize at the pinch-out of the sediments, as is the case in model MSpDéc (Figure 8). Equation 6 shows that ΔL linearly decreases with décollement viscosity and strain rate, and superlinearly increases with overburden thickness ($z_{\mathrm{fftb}}^{'} - z_{\mathrm{fftb}}$). Therefore, decoupling between thin-and thick-skinned deformation is favored if the décollement is weak or the overburden thick, e.g., through stacking of multiple thin-skinned thrust sheets or abundant syn-tectonic sedimentation. A frictionally weak décollement with $\phi_{eff} = 2°$, as used in all models but MSpDéc, is commonly too strong to create efficient decoupling between thin-and thick-skinned tectonics. We only observe efficient decoupling in model MSpHigh and once foreland filling creates a thick foreland basin fill (Figures 7c and 7b), which is readily explained by the above relationship.

Our models and force balance analysis predict (a) a reference thrust sheet length L_{Ref}, (b) thrust sheet lengthening (ΔL) as a function of sedimentation and inherited weaknesses, and (c) decoupling of the foreland-fold-thrust belt and antiformal duplexing of thick-skinned thrust sheets in the hinterland of the foreland belt. L_{Ref} and ΔL are in the same order of magnitude and increase if the crust has a weaker rheology. Our quantification explains why the structural style in many mountain belts on Earth is strongly influenced by inherited weaknesses, sedimentation and weak decoupling horizons. The force balance is a simplified approximation of complex and nonlinear model behavior. In nature, we expect that a combination of the different presented factors influences mountain belt style.

4.3. Model Limitations

Our models are a simplified representation of nature and there are several processes that are not accounted for, notably the effect of varying crustal rheology, precollisional subduction, mantle delamination, and spatially variable surface processes linked to, for instance, orographic effects.

We do not investigate the influence of varying crustal rheology. Jammes and Huismans (2012) investigated the influence of crustal rheology in a similar setup to ours. They show that a weaker upper and middle crust

enhances crustal decoupling, favors outward propagation of structures, promotes retro-wedge loading and accelerates orogenic plateau formation. A stronger upper and middle crust promotes opposing behavior. Many modern orogens, including the Alps, Pyrenees, and Himalaya, are characterized by a rheologically strong lower crust and a detachment level in the middle crust, as used here (Gao et al., 2016; Muñoz, 1992; Replumaz et al., 2010; Schmid et al., 1996). Thus, our rheological model setup is probably to first order representative for these orogenic systems. Liao and Gerya (2017), Liao et al. (2018), Vogt et al. (2018), and Huangfu et al. (2018) show that lateral crustal strength contrasts have a strong influence on the distribution of deformation. Lateral variability in crustal rheology can be invoked if the simple distribution of shortening shown here cannot explain the distribution of shortening in a natural mountain belt (see discussion in comparison to nature section).

Our models do not include full lithospheric break-up with ocean formation, followed by lithospheric cooling, and inversion starting with oceanic subduction. Subduction deflects the temperature field downwards in the vicinity of the subduction zone (J. P. Butler et al., 2013; Wolf & Huismans, 2019), which allows for a transitional phase of continental subduction, UHP rock formation, heating, and exhumation. This early collision phase may create a bigger central, uplifted plug than in our models, as shown by J. P. Butler et al. (2013). Also, deflection of the temperature field by precollisional subduction might temporarily induce a stronger, indenting retro-side, which delays progression of deformation onto the retro-orogen (J. P. Butler et al., 2013). This early collision phase will therefore affect early orogenic structure, but is not expected to change the distribution of shortening during later orogenic growth significantly.

We also do not investigate the influence of a weak or removed upper plate lithospheric mantle. Hyndman et al. (2005) and Currie et al. (2008) show that subduction zones often have a weak and thinned back-arc lithospheric mantle, which seems to be required for back-arc deformation to occur (Wolf & Huismans, 2019). Weakening of the back-arc lithospheric mantle through removal or metasomatism (Chung et al., 2005) unpins the position of the mantle singularity (S-point) and may lead to thrusting of the pro-lithosphere under the retro-plate crust during orogenic growth (Huangfu et al., 2018; Kelly et al., 2016, 2020; Li et al., 2016). Such a process could be operating in the Himalayan-Tibetan orogen, see below.

We only explore the effect of spatially and temporally uniform surface processes on model evolution. Typically, mountain belts create an orographic barrier that can induce differential erosion within a mountain belt, which is shown to have a strong effect on orogenic growth (e.g., Beaumont et al., 2001; Willett, 1999). As will become apparent in the comparison to the Himalaya, spatially nonuniform surface process with high efficiency exert a strong influence on mountain building and have the potential to modify the shortening distribution shown in Figure 9.

4.4. Comparison With Previous Modeling Studies

The large-scale evolution of shortening distribution (e.g., Figure 9) can already be observed in some early S-point models (Beaumont et al., 1994; Vanderhaeghe et al., 2003; Willett & Beaumont, 1994; Willett et al., 1993), as reviewed by Jamieson and Beaumont (2013). The migration of the uplifted plug onto the retro-side of the orogen led Willett and Beaumont (1994) to propose that subduction of Asian lithosphere below India formed the Himalayan-Tibetan orogen, opposite to the nowadays commonly recognized subduction direction (e.g., Nabelek et al., 2009; Owens & Zandt, 1997; Replumaz et al., 2010). Models of these early studies also developed step-up shear zones, a viscous decoupling horizon and a mantle singularity (S-point), which we infer to be the primary controlling factors of model evolution (Figure 9a). This congruence corroborates our model inferences for the controlling factors of model evolution, and shows how early S-point models and newer upper-mantle-scale models, as used here, relate. However, upper-mantle-scale models that include strain-dependent weakening do not necessarily produce a retro-step-up shear zone, which has a profound effect on shortening distribution during orogen growth, as discussed above. Erdős et al. (2014) inferred that extensional inheritance is key to produce retro-wedge deformation, while we can simplify this to the existence of a retro-step-up shear zone. We believe that the latter is likely to exist, given that most mountain belts on Earth include a phase of inversion of inherited weak structures during the initial collision phase. We can furthermore show that slab pull has no primary influence on mountain belt structure, but can provide a force to drive orogenesis, and that internal loading through crustal shortening is the cause for the evolution shown in Figure 9.

Full coupling between fluvial surface processes and tectonics during mountain building was first investigated by Beaumont et al. (1992), followed by a series of modeling studies that looked at the interplay between tectonics and fluvial erosion (Stolar et al., 2006, 2007; Willett, 1999; Willett et al., 2001). These studies focused on mountain belts that reach steady state between tectonic material influx and erosional outflux; they did not have sufficient resolution to include deposition and the interaction between thin-skinned and thick-skinned deformation. Beaumont et al. (2000), Erdős et al. (2014, 2015), and Grool et al. (2019) included a weak décollement horizon in the crust as used here and investigated its influence on relatively small orogenic wedges. Simplified sedimentation and erosion routines are relatively commonplace in geodynamic modeling (e.g., J. P. Butler et al., 2013; Erdős et al., 2014, 2015; Grool et al., 2019; Kelly et al., 2020). However, fully coupled landscape-evolution models and thermo-mechanical models, as we use here, are far less common (e.g., Thieulot et al., 2014; Ueda et al., 2015). This study is the first to show end-member models that investigate the interaction between tectonics and surface processes during mountain growth from small to large, with a 2D mass conserving landscape-evolution model, and including a weak shallow crustal décollement. Using these models, we show how fluvial erosion and deposition modify orogenic growth in terms of width, topography and structural style. The latter is supported by a force-balance analysis that quantifies thrusting during orogenic growth.

5. Comparison to Natural Examples

The comparison of the distribution of shortening and variable structural style during mountain growth predicted by the models (Figures 9 and 10) with natural examples requires well-studied mountain belts with deep reflection seismic surveys and preferably balanced crustal- or lithospheric-scale cross sections. There are only a few mountain belts on Earth that fulfill (some of) these criteria, preventing a statistical comparison of shortening distribution as a function of orogen size with natural examples. Instead, we compare our model inferences to the well-studied Pyrenean, Alpine, and Himalayan-Tibetan orogens, and provide a quantitative comparison of shortening estimates, deformation history, and structural style. Within those mountain belts we will look more specifically at the ECORS-profile in the Pyrenees (Muñoz, 1992), the NFP-20 EAST profile from the western European Alps (Schmid et al., 1996), and the cross section through the southern half of the Himalayan-Tibetan orogen from Nabelek et al. (2009) (Figure 11). For each orogen we first look at similarities to the shortening distribution and influences on structural style derived from our models, before discussing notable differences. We note that compared to the Pyrenees and Alps, the Himalayan-Tibetan orogen is far less comprehensively understood. However, it is the only modern continent-continent collisional orogen containing an elevated plateau, and is thus an important part of this comparison to natural examples.

5.1. Pyrenees

Mesozoic extension resulted in rift-basin formation and mantle exhumation along the Iberia-Europe plate boundary (Jammes et al., 2009; Sibuet et al., 2004; Tugend et al., 2014). Subsequent shortening started in the Late Cretaceous (~80 Ma), peaked during Eocene-Oligocene times and continued into the Miocene (Beaumont et al., 2000; Muñoz, 1992, 2019). Shortening was accommodated by outward-propagating inversion of weak upper crustal extensional structures, and underthrusting of the Iberian lower crust and lithospheric mantle beneath Europe (Beaumont et al., 2000; Muñoz, 1992). The former Iberian margin and several additional crustal thrust sheets form the main body of the mountain belt, and build an antiformal stack known as the Axial Zone (Muñoz, 1992, 2019). Inversion of the former northern hyperextended rift domain forms the narrow North Pyrenean Zone, consisting primarily of inverted extensional blocks (Grool et al., 2018; Teixell et al., 2018). Lherzolite bodies are exposed along the former main extensional detachment between Iberia and Europe. The foreland basins preserve syn-deformational deposits and have a structural style controlled by the distribution of prerift Triassic salt deposits, which form a weak décollement horizon (Muñoz, 1992, 2019). Convergence estimates for the Eastern Pyrenees (ECORS) vary between 90 and 165 km (Beaumont et al., 2000; Grool et al., 2018; Mouthereau et al., 2014; Muñoz, 1992). Shortening is accommodated by inversion of the rift margin extensional faults and newly formed thrust sheets from the Iberian crust (pro-side). On the contrary, no new thrust sheet developed in the undeformed European crust. As most shortening is accommodated in the pro-wedge and the inverted plug, this system can be considered an example of a small PU

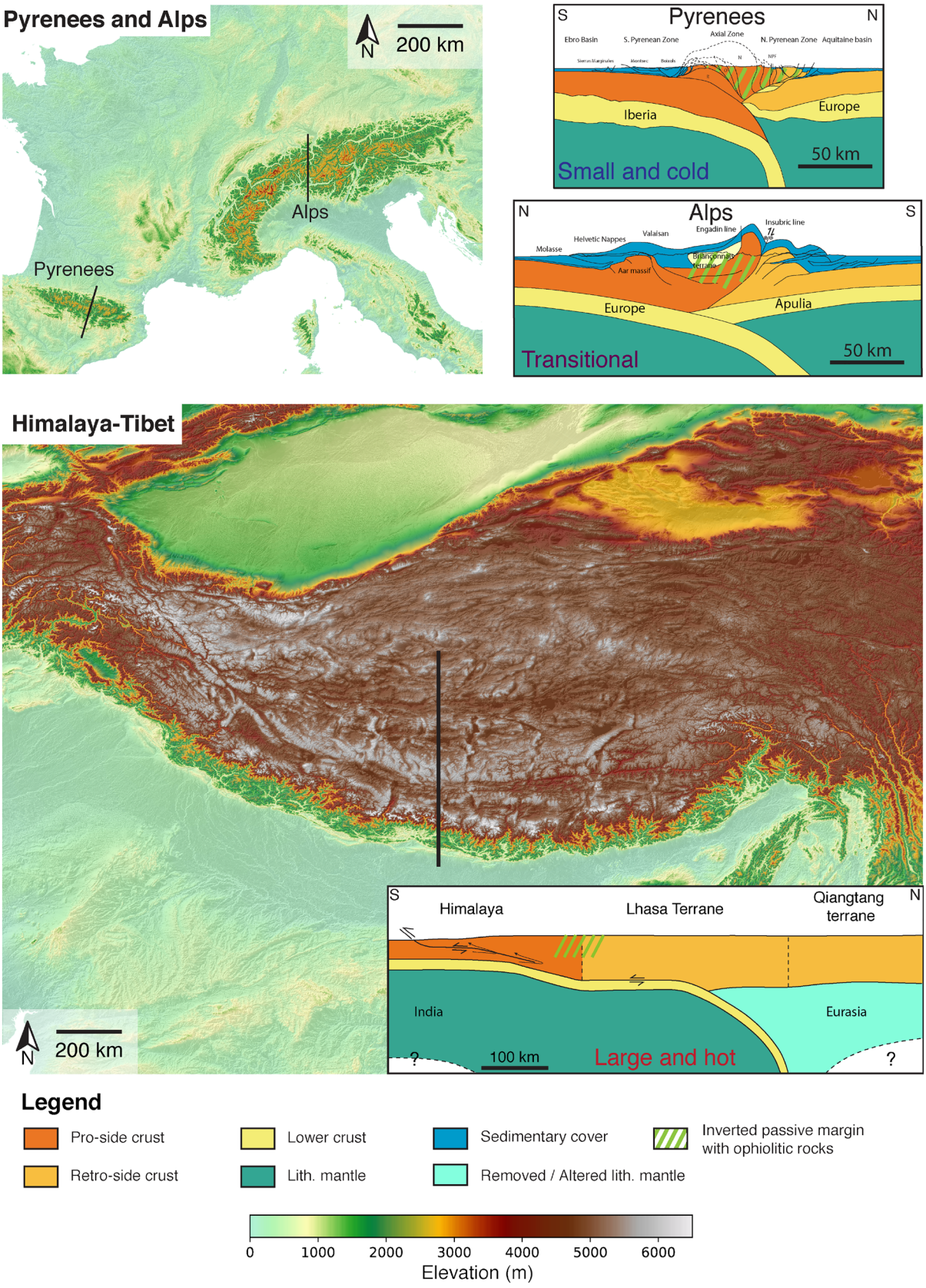
Pyrenees and Alps
N
200 km
Alps
Pyrenees
S
Pyrenees
N
Ebro Basin
S. Pyrenean Zone
Axial Zone
N. Pyrenean Zone
Aquitaine basin
Iberia
Europe
Small and cold
50 km
N
Alps
S
Molasse
Helvetic Nappes
Valaisan
Engadin line
Insubric line
Briançonnais
Aar massif
Europe
Apulia
Transitional
50 km
Himalaya-Tibet
S
Himalaya
Lhasa Terrane
Qiangtang terrane
N
India
Eurasia
100 km
Large and hot
?
?
N
200 km
Legend
Pro-side crust
Retro-side crust
Lower crust
Lith. mantle
Sedimentary cover
Removed / Altered lith. mantle
Inverted passive margin with ophiolitic rocks
0
1000
2000
3000
4000
5000
6000
Elevation (m)

orogenic wedge (Figure 9). The antiformal stack is related to a salt-detached foreland fold-thrust belt, as shown in model MSpDéc and quantified in (Figure 10d). As the occurrence of antiformal stacking depends on the thickness of the foreland fold-thrust belt (see model MSpDéc), supra-salt, syn-extensional deposits potentially enhanced antiformal stack formation already at the start of orogenesis. The exhumed Lherzolite bodies document crustal thinning and mantle exhumation before mountain building in the Pyrenees, as seen in MExt.

5.2. Alps

Orogenesis in the Central Alps results from a complex tectonic and paleogeographic evolution during collision of Europe and Adria. Subduction of the Piemont-Liguria ocean and northward movement of Adria led to early nappe stacking, terrane accretion, subduction of the European passive margin, UHP metamorphism, and subsequent exhumation of UHP-metamorphic rocks through the late Eocene (~35 Ma). The ensuing continent-continent collision is characterized by subduction of the European lower crust and mantle lithosphere, bivergent orogenic thrusting, and underthrusting of the Adriatic lower crust and lithospheric mantle below the orogenic wedge (Handy et al., 2010; Rosenberg & Kissling, 2013; Schmid et al., 2004, 2017; Stampfli et al., 1998, see Figure 11). Reconstructing the amount of crustal shortening and plate convergence is difficult, especially for the early (pre 35 Ma) nappe stacking phase. Some convergence estimates are (a) ~160 km since 40 Ma for profile NFP-20 East (Figure 11; Schmid et al., 1996), (b) 98 km for post 35 Ma collision for the same profile (Rosenberg & Kissling, 2013), and (c) 165 km for post 35 Ma collision a bit SW of the NFP-20 East profile (Schmid et al., 2017). As these estimates do not include the early nappe-stacking phase, cumulative convergence for the profile presented in Figure 11 is certainly greater than 150 km. Our models with low to medium surface-process efficiency require 200–300 km of convergence of normal crustal thickness plates to produce an orogen with a size comparable to the Central Alps. The amount of crustal shortening and retro-wedge deformation in the Central and Western Alps decreases systematically toward the SW (Bellahsen et al., 2014; Schmid et al., 2017). These lateral variations potentially document the shift from a small PU wedge in the SW to a PUR wedge with significant retro-wedge shortening and underthrusting of the retro-wedge lower crust and lithospheric mantle in the Central Alps. The Central and Western Alps also show antiformal thrust-sheet stacking in the hinterland of the salt-detached Jura fold-thrust belt (Schmid & Kissling, 2000; Schmid et al., 2004), as seen in model M6, and explained in our force balance analysis (Figure 10d). Our models do not include precollision subduction, UHP rock formation and exhumation. As shown by J. P. Butler et al. (2013), exhumed UHP rocks become part of the central uplifted plug (U). Liao and Gerya (2017), Liao et al. (2018), and Vogt et al. (2018) attribute variable retro-wedge deformation in the Western Alps to the rheological contrast induced by the Ivrea mantle body, which was exhumed during precollisional extension and remained at upper crustal levels during collision. Our models suggest that the limited retro-wedge deformation in the Western Alps may also be a natural consequence of limited crustal shortening resulting in dominantly pro-wedge deformation.

5.3. Himalayan-Tibetan Orogen

During the Mesozoic, the Tibetan Plateau was assembled by the successive accretion of several terranes (Figure 11; Kapp & DeCelles, 2019; Yin & Harrison, 2000). Subduction of the Indian oceanic slab during the Mesozoic and early Paleogene led to collision of thinned Indian lithosphere at ~59 Ma (DeCelles et al., 2014; Hu et al., 2015). Collision of normal thickness lithosphere started at around 50 to 45 Ma (Guillot et al., 2003; Kapp & DeCelles, 2019; Negredo et al., 2007; Replumaz & Tapponnier, 2003). Total post ~59 Ma convergence estimates vary greatly and are in the order of 2,900 ± 750 km (Dupont-Nivet et al., 2010; Guillot & Replumaz, 2013). Guillot and Replumaz (2013) quantify convergence accommodated within the pro-plate to 1,500 ± 300 km, versus > 1100 km within the Tibetan retro-plate, giving a distribution of 58% pro- and 42% ret-

Figure 11. Digital elevation model (DEM) of the Pyrenees, European Alps, and Himalaya-Tibet orogen and corresponding cross sections. The two DEMs have the same colorbar and scale. The Pyrenees is an example of a small and cold orogen (cross section modified from Muñoz [1992]), the Western Alps, although variable along strike, might be an example of a transitional orogen (cross section modified from Schmid et al. [1996]), and the Himalaya-Tibet orogen is the only recent example of a large and hot continent-continent collision orogen (cross section modified from Nabelek et al. [2009]). Crustal units and structures in the Himalaya-Tibet orogen are strongly simplified, also omitting a differentiation between crust and sedimentary cover. The lower bounds of the Indian and Eurasian lithospheric mantles are inferred from Owens and Zandt (1997). The Pyrenean and Alpine cross sections have the same scale but are flipped North-South.

ro-wedge shortening since the onset of continent-continent collision. The southern, Himalayan, foreland fold-thrust belt records shortening, estimated from cross-section balancing, of 500–750 km (DeCelles et al., 2001; Long et al., 2011; Robinson, 2008). Antiformal crustal duplexing is inferred in the back of the foreland fold-thrust belt (Gao et al., 2016). Thrusting and crustal shortening in the Qiangtang and Lhasa terranes started already in Late-Cretaceous times, before onset of continent-continent collision (DeCelles et al., 2002; Kapp et al., 2003, 2005; Volkmer et al., 2007; Wang et al., 2014). Therefore, India collided with already thickened crust of an Andean-type orogen, which may have formed a plateau (Lhasaplano) during Late-Cretaceous—Eocene times (Kapp & DeCelles, 2019; Kapp et al., 2007). Thermochronological data indicate that a high plateau with low erosion rates was probably established in Tibet by Eocene times (Rohrmann et al., 2012; van der Beek et al., 2009), consistent with 26–27 Ma high-elevation paleoaltimetry dating in the center of the Tibetan Plateau (DeCelles et al., 2007; Molnar et al., 2010). Low erosion rates in the dry Tibetan Plateau stand in stark contrast to monsoon-driven high erosion and exhumation rates in the frontal part of the Himalaya (e.g., Burbank et al., 1996; Herman et al., 2010; Lavé & Avouac, 2001; Wobus et al., 2003). During continent-continent collision, thrust activity propagated to first order from the possibly pre-thickened Qiangtang terrane toward the Tibetan Plateau margins (see review in Kapp & DeCelles, 2019; Wang et al., 2014). This explains significant northward translation of the India-Asia suture during early continent-continent collision (DeCelles et al., 2002; Yi et al., 2011). However, simultaneous shortening in spatially very different locations for instance at the India-Asia suture zone and in the Qiangtang terrane is documented (Kapp & DeCelles, 2019). Shortening included (consecutive) magmatic "sweeps" and "jumps," possibly connected to removal of mantle lithosphere pieces genetically related to the accreted terranes (Chung et al., 2005; Kapp & DeCelles, 2019; Kelly et al., 2020; Liu et al., 2014). Furthermore, facilitated by a weak or removed Tibetan lithospheric mantle, the present day Indian lithospheric mantle and lower crust have thrust far under the orogen, leading to a position of the S-point below the accreted Tibetan terranes and not below thickened Indian crust (Figure 11; Nabelek et al., 2009; Owens & Zandt, 1997).

Our models and the inferred shortening distribution as a function of convergence can explain the first-order characteristics of the Himalaya-Tibet orogen as a plateau flanked by wedges (Figure 9), decoupling of overthickened crust from the lithospheric mantle, and independent evolution of crust and mantle lithosphere. Crustal underthrusting and duplexing in the hinterland of the thick Himalayan foreland fold-thrust belt (Gao et al., 2016) fits well with the predictions of our force balance analysis (Figure 10d). Furthermore, the distribution of shortening as compiled by Guillot and Replumaz (2013) is consistent with values inferred from our models. However, the sketch shown in Figure 9d clearly does not match the present day structure of the Himalayan-Tibetan orogen. Especially the position of the India-Asia suture zone and the present day S-point position of the Indian plate are reversed in comparison to our model evolution and require explanation. Recent modeling studies (Huangfu et al., 2018; Kelly et al., 2016, 2020; Li et al., 2016) show that several key aspects of Himalayan mountain building can be explained by continent-continent collision, including delamination tectonics facilitated by strength and density contrasts in the lithospheric mantle genetically related to accreted terranes. Kelly et al. (2020) propose that indentation of India induces initiation of shortening in the North part of the Qiangtang terrane, facilitated by a weak Qiangtang-lithospheric mantle, followed by lateral North-South spreading of shortening similar to our models. Lateral growth is accompanied by peeling and removal of several lithospheric mantle pieces, creating space for late underthrusting of the buoyant Indian lithospheric mantle. High erosion and exhumation rates at the Himalayan mountain front (e.g., Burbank et al., 1996; Herman et al., 2010; Lavé & Avouac, 2001) counteract accumulation of Indian crustal material and reduce the contribution of pro-side material to the mountain belt. These modeling studies highlight that rheological decoupling between crust and lithospheric mantle can lead to a strongly independent evolution of the crust and mantle in large and hot orogens. However, the above modeling studies do not investigate the influence of a pre-thickened Cordilleran-type orogen on the retro-plate during continent-continent collision. Crustal thickening in Cordilleran-type orogens like the Andes is typically related to removal of the overriding plate lithospheric mantle in Rayleigh-Taylor instabilities (DeCelles et al., 2009; Schurr et al., 2006; Wolf & Huismans, 2019). Precollision removal of the Asian lithospheric mantle would facilitate underthrusting of the Indian lithosphere during continent-continent collision, translating the S-point beneath the upper plate. This could be a modified explanation for the large-scale lithospheric evolution of the Himalaya-Tibet orogen, which does not require peeling and removal of several pieces of lithospheric mantle. Hence, initiation of shortening in the Qiangtang terrane or collision with a preexisting orogen, efficient erosion of Himalayan crustal

material, removal of retro-lithospheric mantle and underthrusting of the Indian lower lithosphere can explain the first order differences between nature and our presented model evolution.

6. Conclusions

We have used thermo-mechanical models coupled to a surface process model to investigate the effects of mantle-lithosphere density, extensional inheritance, surface-process efficiency, and decoupling between thin-and thick-skinned tectonics, on orogen growth from small and cold to large and hot. We have also derived a force-balance analysis of thrust formation during orogenic growth and compared our model inferences to the Pyrenees, Alps, and Himalayas to draw the following conclusions:

We find a relationship between orogen size and distribution of shortening in terms of pro-versus retro-wedge deformation: (1) Small and cold orogens with cross-sectional area $< 3.75 \times 10^9$ m^2, corresponding to at most 150 km of convergence in our reference model, are expected to form a mountain belt in which deformation is mainly localized on the pro-side and within (inverted) structures from the early collision stage, forming the uplifted plug. (2) Transitional orogens with 3.75×10^9 m^2 < CA < $\sim 12.5 \times 10^9$ m^2 (150–500 km of collisional convergence in the reference model) are expected to additionally exhibit thick-skinned retro-wedge deformation. (3) If crustal shortening creates CA > $\sim 12.5 \times 10^9$ m^2, a large and hot plateau forms, located mostly on the retro-side as a consequence of underthrusting of the retro-mantle. The onset of plateau formation is additionally dependent on radioactive heat production and the timescale of thermal equilibration of the crust.

The shortening distribution in orogens as they evolve from small and cold to large and hot is controlled by internal crustal loading. Slab pull of the subducting lithosphere can provide a driving force of orogenesis but does not affect the distribution and structural style of deformation. Precollisional extensional inheritance results in emplacement of mantle material close to the surface and a structural domain dominated by inversion tectonics, but provides only a secondary control on large-scale mountain-belt development. Increased orogenic topography enhances erosion such that mountain-belt growth is delayed as a function of orogen size and surface-process efficiency. Strong erosion in the orogen core is linked to deep, overfilled foreland basins. Limited exhumation characterizes low surface-process efficiency, while exhumation of deep crustal rocks characterizes high surface-process efficiency. Only very high surface-process efficiency can induce flux steady state between crustal accretion and erosion.

The force-balance analysis explains variable structural styles of orogenic growth as a function of inherited weaknesses, sedimentation and (de-)coupling between thin-and thick-skinned deformation. A reference thrust spacing can be defined and depends on crustal strength and mid-crustal viscosity. Thrust spacing is amplified by syntectonic sedimentation or inherited weaknesses, which are also expected to modify the structural style of the mountain belt. A weak décollement horizon and thick foreland fold-thrust belt efficiently decouple thin- and thick-skinned deformation. Decoupled systems are characterized by a stacked foreland fold-thrust belt recording significant deformation, and crustal underthrusting leading to antiformal duplexing in the hinterland of the thin-skinned belt.

Comparison with the Pyrenees, Alps, and Himalaya shows the applicability but also the limitations of the idealized evolutionary sequence developed here. The Pyrenees and Alps exhibit the first two characteristic phases identified here, and show further similarities with model evolution and derived structural style. We cannot reproduce the complex deformation history of the Himalaya, however, possibly because our model does not take lithospheric delamination of inherited accreted terranes or precollisional thickening into account. Yet, the large and hot Himalayan-Tibetan orogen shows some of the first-order characteristics and structural styles presented here for orogens with the largest amounts of shortening.

Appendix A: Modelling Methods

A1 Thermo-Mechanical Model

We use the modified 2-dimensional Arbitrary Lagrangian-Eulerian (ALE), thermo-mechanically coupled finite element code FANTOM (Thieulot, 2011; Wolf & Huismans, 2019), coupled to the surface process

model Fastscape (Braun & Willett, 2013; Yuan et al., 2019, see Section A3), to investigate the dynamics of orogenic growth as a function of convergence. The thermo-mechanical model computes momentum and mass conservation (Appendixes A1 and A2) of plane-strain incompressible creeping fluids, and heat transport (Appendix A3) in the model domain:

$$\frac{\partial \sigma_{ij}}{\partial x_i} + \rho g = 0 \quad i,j = 1,2, \tag{A1}$$

$$\frac{\partial v_i}{\partial x_i} = 0 \quad i = 1,2, \tag{A2}$$

$$c_p \rho \left(\frac{\partial T}{\partial t} + v_i \frac{\partial T}{\partial x_i} \right) = k \frac{\partial}{\partial x_i} \frac{\partial T}{\partial x_i} + H + v_j \alpha \rho T g, \tag{A3}$$

where v_i are velocity components, x_i are spatial coordinates, σ_{ij} is the stress tensor, ρ is density, g is gravitational acceleration, c_p is specific heat, T is temperature, t is time, k is thermal conductivity, H is radioactive heat production per unit volume, α is the volumetric thermal expansion coefficient. The last term in Equation A3 is the correction for adiabatic heating when material moves vertically. The density ρ changes as a function of the thermal expansion coefficient α.

Model materials deform either by frictional-plastic or by viscous flow. Frictional-plastic behavior is modeled using a pressure dependent Drucker-Prager yield criterion

$$\sigma'_{plast} = P \cdot \sin(\phi_{eff}) + C \cdot \cos(\phi_{eff}), \tag{A4}$$

where σ'_{plast} is the square root of the second invariant of the deviatoric stress, P is the dynamic pressure, ϕ_{eff} is the effective angle of internal friction and C is cohesion. Strain-weakening is accounted for by linearly reducing ϕ_{eff} from 15° to 2° and C from 20 to 4 MPa through a predefined plastic strain ($\varepsilon_{\text{plastic}}$) interval $0.1 < \varepsilon_{\text{plastic}} < 1.1$ (Huismans & Beaumont, 2003).

Viscous deformation is described by a nonlinear, thermally activated power law creep formulation which relates pressure, temperature and strain rate to the viscous flow stress, σ'_{visc}:

$$\sigma'_{visc} = f \cdot A^{-\frac{1}{n}} \cdot (\dot{\epsilon}_{eff})^{\frac{1}{n}} \cdot exp\left(\frac{Q + VP}{nRT} \right), \tag{A5}$$

where σ'_{visc} is the square root of the second invariant of the deviatoric stress, $\dot{\epsilon}_{eff}$ is the square root of the second invariant of the deviatoric strain rate, f is a scaling factor, A the preexponential factor converted to plane strain, n the power-law exponent, Q activation energy, V activation volume, P the dynamic pressure, and R the universal gas constant.

At high pressures, high differential stresses, and low temperatures, olivine mainly deforms by a temperature-insensitive exponential (Peierl's) creep (Katayama & Karato, 2008; Tsenn & Carter, 1987). We approximate this deformation mechanism by limiting the flow stress of all model materials based on the wet olivine flaw to $\sigma'_{\text{plast}} \leq 300$ MPa (e.g., Andrews & Billen, 2009; J. P. Butler et al., 2015).

A2 Model Geometry and Boundary Conditions

Continent-continent collision is modeled using an idealized upper mantle domain with 1,200 km horizontal and 600 km vertical extent (Figure 1, Table 1). The model domain has a typical layered setup of 25 km of upper/mid crust, 10 km lower crust, and 85 km lithospheric mantle down to 120 km, overlying the sublithospheric upper mantle (see Section 2.1 for detailed information).

The initial temperature distribution in the model domain represents typical Phanerozoic values and is at steady state, with a Moho temperature of 550°C and 1,330°C at the base of the lithosphere, resulting in a

surface heat flow of 53 mW m^{-2} and heat flux in the sublithospheric mantle of 20.8 mW m^{-2}. To mimic mantle convection at high Nusselt number, and to maintain the heat flux at the lithosphere-asthenosphere boundary k linearly increases from 2.25 to 52.0 W m^{-1} K^{-1} between 1,330 and 1,340°C in the sublithospheric mantle (Pysklywec & Beaumont, 2004). The values are scaled to keep an adiabatic gradient of 0.4°C km^{-1} in the sublithospheric domain. All other materials have a thermal conductivity k = 2.25 Wm^{-1} K^{-1}. The side boundaries are insulated and the top and bottom boundaries have a constant temperature boundary condition of respectively 0°C and 1,522°C.

Continent-continent collision is modeled by applying velocity boundary conditions on the model sides. Inflow of lithospheric material is balanced by a small distributed outflow in the sublithospheric mantle. The upper surface is stress free, and the lower and side boundaries have free slip conditions.

The Eulerian grid consists of 1,600 cells in the horizontal and 323 cells in the vertical direction. The distribution of cells is nonuniform in the vertical direction, with 100 cells in the uppermost 25 km, 135 cells in the following 135 km, and 88 cells in the lowermost 440 km. This leads to vertical resolutions of 250 m, 1 km, and 5 km respectively, and a uniform horizontal resolution of 750 m. Eulerian cells are initially filled with five uniformly spaced Lagrangian particles. During model evolution, particle numbers per cell are kept between minimum 5 and maximum 50.

A3 Surface Process Model

We use the 2-dimensional, finite difference, implicit, O(n) surface process code Fastscape (Braun & Willett, 2013) which has been extended by a continental sediment transport and deposition term (Yuan et al., 2019) to model erosion and mass conserving deposition:

$$\frac{\partial h}{\partial t} = U - K_f A^m S^n + K_c \nabla^2 h + \frac{G}{A}\int_A (U - \frac{\partial h}{\partial t}) dA, \tag{A6}$$

h is surface elevation, t is time, U is the uplift rate, K_f is the fluvial erosion coefficient, A is catchment area upstream, S is the local slope, m, n are the stream power law exponents, K_c is the hillslope diffusion coefficient, and G is a deposition coefficient. The model accounts for a change in topography as a function of uplift, Stream-power law erosion (K_f-term), hillslope creep (K_c-term), and continental deposition as a function of the average erosion upstream. We additionally account for mass conserving filling of local minima, i.e. lakes and the orogenic foreland basin, by filling up from the deepest point of the local minimum according to the available sediments. All rivers are connected to either the left or right side boundary by bridging local minima to their lowest neighbor catchment.

The two codes are fully coupled in a T-coupling manner (Beaumont et al., 1992). After each mechanical timestep of FANTOM, the resulting 1D surface velocity is given to Fastscape as a cylindrical 2D signal. First the Fastscape surface is advected horizontally according to the given horizontal velocity field. Subsequently Equation A6 is solved with U being the vertical velocity signal. Finally, the average Fastscape elevation is given back as new free-surface to the mechanical code and time-stepping continues. In FANTOM areas above the old free surface are filled with sediment which has the same rheological and density properties as upper crust, but a different color (see Figure 1)

A4 Calculation of Tectonic Force and Lithospheric Pull

The tectonic boundary force F_{TBF} is defined as

$$F_{TBF} = \int_0^{z_{lab}} \sigma'_{xx} dz = \int_0^{z_{lab}} 2\dot{\epsilon}_{xx}\mu_{eff} dz, \tag{A7}$$

where z_{lab} is lithosphere thickness, σ'_{xx} is horizontal deviatoric stress, $\dot{\epsilon}_{xx}$ is horizontal strain rate, and μ_{eff} is effective viscosity. We calculate F_{TBF} at the sides of the model with z_{lab} = 120 km. Net pull, i.e., tensional stresses, are defined as positive. The tectonic force is the net force resulting from the given boundary conditions, lithospheric pull or push, and resisting forces.

Lithospheric pull is calculated as the area-integrated density difference between slab material (i.e., metamorphosed lower crust and lithospheric mantle), and sublithospheric mantle. All lithospheric material below the lower bound of the lithospheric mantle is considered to contribute to slab pull and part of the computation.

Appendix B: Supplementary Material

Supplementary material includes:

- Supplementary Models SM1 to SM6
- Fastscape surfaces of models M5, M6, and M7
- Diagram highlighting mountain belt development normalized to S-point
- Animations of all models

Data Availability Statement

Data are computed with the equations presented here and videos of all model runs can be found under https://doi.org/10.6084/m9.figshare.13347260.

Acknowledgments
This research is supported by TOTAL, through the project "Coupling lithosphere deformation and surface processes (COLORS)." We thank Uninett Sigma2 for computing time of project NN4704K. Many thanks to Jean Braun and Xiaoping Yuan for helping with the coupling of Fastscape to FANTOM. Isabelle Manighetti and Peter G. DeCelles are thanked for very helpful comments and editorial handling, two anonymous reviewers are thanked for constructive reviews. Thomas Theunissen, Gang Lu, and the whole COLORS team are thanked for fruitful discussions.

References

Amilibia, A., Sabat, F., McClay, K. R., Munoz, J. A., Roca, E., & Chong, G. (2008). The role of inherited tectono-sedimentary architecture in the development of the central Andean mountain belt: Insights from the Cordillera de Domeyko. *Journal of Structural Geology*, *30*(12), 1520–1539. https://doi.org/10.1016/j.jsg.2008.08.005

Andrews, E. R., & Billen, M. I. (2009). Rheologic controls on the dynamics of slab detachment. *Tectonophysics*, *464*(1–4), 60–69. https://doi.org/10.1016/j.tecto.2007.09.004

Beaumont, C., Ellis, S., & Pfiffner, A. (1999). Dynamics of sediment subduction-accretion at convergent margins: Short-term modes, long-term deformation, and tectonic implications. *Journal of Geophysical Research*, *104*(B8), 17573–17601. https://doi.org/10.1029/1999jb900136

Beaumont, C., Fullsack, P., & Hamilton, J. (1992). Erosional control of active compressional orogens. In K. R., McClay (Ed.), *Thrust tectonics* (pp. 1–18). Dordrecht: Springer. https://doi.org/10.1007/978-94-011-3066-0_1

Beaumont, C., Fullsack, P., & Hamilton, J. (1994). Styles of crustal deformation in compressional orogens caused by subduction of the underlying lithosphere. *Tectonophysics*, *232*(1–4), 119–132. https://doi.org/10.1016/0040-1951(94)90079-5

Beaumont, C., Jamieson, R. A., Nguyen, M. H., & Lee, B. (2001). Himalayan tectonics explained by extrusion of a low-viscosity crustal channel coupled to focused surface denudation. *Nature*, *414*(6865), 738–742. https://doi.org/10.1038/414738a

Beaumont, C., Munoz, J. A., Hamilton, J., & Fullsack, P. (2000). Factors controlling the Alpine evolution of the central Pyrenees inferred from a comparison of observations and geodynamical models. *Journal of Geophysical Research*, *105*(B4), 8121–8145. https://doi.org/10.1029/1999jb900390

Beaumont, C., Nguyen, M. H., Jamieson, R. A., & Ellis, S. (2006). Crustal flow modes in large hot orogens. *Geological Society, London, Special Publications*, *268*(1), 91–145. https://doi.org/10.1144/GSL.SP.2006.268.01.05

Becker, T. W., & Faccenna, C. (2011). Mantle conveyor beneath the Tethyan collisional belt. *Earth and Planetary Science Letters*, *310*(3–4), 453–461. https://doi.org/10.1016/j.epsl.2011.08.021

Bellahsen, N., Mouthereau, F., Boutoux, A., Bellanger, M., Lacombe, O., Jolivet, L., & Rolland, Y. (2014). Collision kinematics in the western external Alps. *Tectonics*, *33*(6), 1055–1088. https://doi.org/10.1002/2013tc003453

Braun, J. (2006). Recent advances and current problems in modelling surface processes and their interaction with crustal deformation. *Geological Society, London, Special Publications*, *253*(1), 307–325. https://doi.org/10.1144/gsl.Sp.2006.253.01.16

Braun, J., & Beaumont, C. (1995). Three-dimensional numerical experiments of strain partitioning at oblique plate boundaries: Implications for contrasting tectonic styles in the southern Coast Ranges, California, and central South Island, New Zealand. *Journal of Geophysical Research*, *100*(B9), 18059–18074. https://doi.org/10.1029/95jb01683

Braun, J., & Willett, S. D. (2013). A very efficient O(n), implicit and parallel method to solve the stream power equation governing fluvial incision and landscape evolution. *Geomorphology*, *180*, 170–179. https://doi.org/10.1016/j.geomorph.2012.10.008

Burbank, D. W., Leland, J., Fielding, E., Anderson, R. S., Brozovic, N., Reid, M. R., & Duncan, C. (1996). Bedrock incision, rock uplift and threshold hillslopes in the northwestern Himalayas. *Nature*, *379*(6565), 505–510. https://doi.org/10.1038/379505a0

Butler, J. P., Beaumont, C., & Jamieson, R. A. (2011). Crustal emplacement of exhuming (ultra) high-pressure rocks: Will that be pro- or retro-side? *Geology*, *39*(7), 635–638. https://doi.org/10.1130/G32166.1

Butler, J. P., Beaumont, C., & Jamieson, R. A. (2013). The Alps 1: A working geodynamic model for burial and exhumation of (ultra) high-pressure rocks in Alpine-type orogens. *Earth and Planetary Science Letters*, *377*, 114–131. https://doi.org/10.1016/j.epsl.2013.06.039

Butler, J. P., Beaumont, C., & Jamieson, R. A. (2015). Paradigm lost: Buoyancy thwarted by the strength of the Western Gneiss Region (ultra) high-pressure terrane, Norway. *Lithosphere*, *7*(4), 379–407. https://doi.org/10.1130/L426.1

Butler, R. W. H., Tavarnelli, E., & Grasso, M. (2006). Structural inheritance in mountain belts: An Alpine-Apennine perspective. *Journal of Structural Geology*, *28*(11), 1893–1908. https://doi.org/10.1016/j.jsg.2006.09.006

Capitanio, F. A., Morra, G., Goes, S., Weinberg, R. F., & Moresi, L. (2010). India-Asia convergence driven by the subduction of the Greater Indian continent. *Nature Geoscience*, *3*(2), 136–139. https://doi.org/10.1038/Ngeo725

Carrera, N., & Muñoz, J. A. (2013). Thick-skinned tectonic style resulting from the inversion of previous structures in the southern Cordillera Oriental (NW Argentine Andes). *Geological Society, London, Special Publications*, *377*(1), 77–100. https://doi.org/10.1144/sp377.2

Carrera, N., Muñoz, J. A., Sabat, F., Mon, R., & Roca, E. (2006). The role of inversion tectonics in the structure of the Cordillera Oriental (NW Argentinean Andes). *Journal of Structural Geology*, *28*(11), 1921–1932. https://doi.org/10.1016/j.jsg.2006.07.006

Chung, S. L., Chu, M. F., Zhang, Y. Q., Xie, Y. W., Lo, C. H., Lee, T. Y., et al. (2005). Tibetan tectonic evolution inferred from spatial and temporal variations in post-collisional magmatism. *Earth-Science Reviews*, *68*(3–4), 173–196. https://doi.org/10.1016/j.earscirev.2004.05.001

Cloos, M. (1993). Lithospheric buoyancy and collisional orogenesis: Subduction of oceanic plateaus, continental margins, island arcs, spreading ridges, and seamounts. *Geological Society of America Bulletin*, *105*(6), 715–737. https://doi.org/10.1130/0016-7606(1993)105⟨0715:Lbacos⟩2.3.Co;2

Cooper, M. A., & Williams, G. D. (Eds.). (1989). *Inversion Tectonics (Vol. 44)*. Geological Society, London, Special Publications. https://doi.org/10.1144/gsl.Sp.1989.044.01.01

Cowie, P. A., Whittaker, A. C., Attal, M., Roberts, G., Tucker, G. E., & Ganas, A. (2008). New constraints on sediment-flux-dependent river incision: Implications for extracting tectonic signals from river profiles. *Geology*, *36*(7), 535–538. https://doi.org/10.1130/G24681a.1

Currie, C. A., Huismans, R. S., & Beaumont, C. (2008). Thinning of continental backarc lithosphere by flow-induced gravitational instability. *Earth and Planetary Science Letters*, *269*(3–4), 435–446. https://doi.org/10.1016/j.epsl.2008.02.037

Dahlen, F. A. (1984). Noncohesive critical Coulomb wedges: An exact solution. *Journal of Geophysical Research*, *89*(B12), 125–133. https://doi.org/10.1029/JB089iB12p10125

Davis, D., Suppe, J., & Dahlen, F. A. (1983). Mechanics of fold-and-thrust belts and accretionary wedges. *Journal of Geophysical Research*, *88*(B2), 1153–1172. https://doi.org/10.1029/JB088iB02p01153

DeCelles, P. G., Ducea, M. N., Kapp, P., & Zandt, G. (2009). Cyclicity in Cordilleran orogenic systems. *Nature Geoscience*, *2*(4), 251–257. https://doi.org/10.1038/Ngeo469

DeCelles, P. G., Kapp, P., Gehrels, G. E., & Ding, L. (2014). Paleocene-Eocene foreland basin evolution in the Himalaya of southern Tibet and Nepal: Implications for the age of initial India-Asia collision. *Tectonics*, *33*(5), 824–849. https://doi.org/10.1002/2014tc003522

DeCelles, P. G., Quade, J., Kapp, P., Fan, M. J., Dettman, D. L., & Ding, L. (2007). High and dry in central Tibet during the Late Oligocene. *Earth and Planetary Science Letters*, *253*(3–4), 389–401. https://doi.org/10.1016/j.epsl.2006.11.001

DeCelles, P. G., Robinson, D. M., Quade, J., Ojha, T. P., Garzione, C. N., Copeland, P., & Upreti, B. N. (2001). Stratigraphy, structure, and tectonic evolution of the Himalayan fold-thrust belt in western Nepal. *Tectonics*, *20*(4), 487–509. https://doi.org/10.1029/2000tc001226

DeCelles, P. G., Robinson, D. M., & Zandt, G. (2002). Implications of shortening in the Himalayan fold-thrust belt for uplift of the Tibetan Plateau. *Tectonics*, *21*(6), https://doi.org/10.1029/2001tc001322

Dupont-Nivet, G., van Hinsbergen, D. J. J., & Torsvik, T. H. (2010). Persistently low Asian paleolatitudes: Implications for the India-Asia collision history. *Tectonics*, *29*, TC5016. https://doi.org/10.1029/2008tc002437

Ellis, S., & Beaumont, C. (1999). Models of convergent boundary tectonics: Implications for the interpretation of Lithoprobe data. *Canadian Journal of Earth Sciences*, *36*(10), 1711–1741. https://doi.org/10.1139/e99-075

Erdős, Z., Huismans, R. S., & van der Beek, P. (2015). First-order control of syntectonic sedimentation on crustal-scale structure of mountain belts. *Journal of Geophysical Research: Solid Earth*, *120*(7), 5362–5377. https://doi.org/10.1002/2014jb011785

Erdős, Z., Huismans, R. S., van der Beek, P., & Thieulot, C. (2014). Extensional inheritance and surface processes as controlling factors of mountain belt structure. *Journal of Geophysical Research: Solid Earth*, *119*(12), 9042–9061. https://doi.org/10.1002/2014jb011408

Fillon, C., Huismans, R. S., & van der Beek, P. (2013). Syntectonic sedimentation effects on the growth of fold-and-thrust belts. *Geology*, *41*(1), 83–86. https://doi.org/10.1130/G33531.1

Forsyth, D., & Uyeda, S. (1975). Relative importance of driving forces of plate motion. *Geophysical Journal of the Royal Astronomical Society*, *43*(1), 163–200. https://doi.org/10.1111/j.1365-246X.1975.tb00631.x

Gao, R., Lu, Z. W., Klemperer, S. L., Wang, H. Y., Dong, S. W., Li, W. H., & Li, H. Q. (2016). Crustal-scale duplexing beneath the Yarlung Zangbo suture in the western Himalaya. *Nature Geoscience*, *9*(7), 555–560. https://doi.org/10.1038/ngeo2730

Gillcrist, R., Coward, M., & Mugnier, J.-L. (1987). Structural inversion and its controls: Examples from the Alpine foreland and the French Alps. *Geodinamica Acta*, *1*(1), 5–34. https://doi.org/10.1080/09853111.1987.11105122

Gleason, G. C., & Tullis, J. (1995). A flow law for dislocation creep of quartz aggregates determined with the molten-salt cell. *Tectonophysics*, *247*(1–4), 1–23. https://doi.org/10.1016/0040-1951(95)00011-B

Grier, M. E., Salfity, J. A., & Allmendinger, R. W. (1991). Andean reactivation of the Cretaceous Salta rift, northwestern Argentina. *Journal of South American Earth Sciences*, *4*(4), 351–372. https://doi.org/10.1016/0895-9811(91)90007-8

Griffin, W., O'Reilly, S. Y., Ryan, C. G., Gaul, O., & Ionov, D. A. (1998). Secular variation in the composition of subcontinental lithospheric mantle: Geophysical and geodynamic implications. In J. Braun, J. Dooley, B. Goleby, et al. (Eds.), *Structure and Evolution of the Australian Continent* (Vol. 26, pp. 1–26). https://doi.org/10.1002/9781118670095.ch1

Grool, A. R., Ford, M., Verges, J., Huismans, R. S., Christophoul, F., & Dielforder, A. (2018). Insights into the crustal-scale dynamics of a doubly vergent orogen from a quantitative analysis of its forelands: A case study of the Eastern Pyrenees. *Tectonics*, *37*(2), 450–476. https://doi.org/10.1002/2017tc004731

Grool, A. R., Huismans, R. S., & Ford, M. (2019). Salt decollement and rift inheritance controls on crustal deformation in orogens. *Terra Nova*, *31*(6), 562–568. https://doi.org/10.1111/ter.12428

Guillot, S., Garzanti, E., Baratoux, D., Marquer, D., Maheo, G., & de Sigoyer, J. (2003). Reconstructing the total shortening history of the NW Himalaya. *Geochemistry, Geophysics, Geosystems*, *4*(7). https://doi.org/10.1029/2002gc000484

Guillot, S., & Replumaz, A. (2013). Importance of continental subductions for the growth of the Tibetan Plateau. *Bulletin de la Societe Geologique de France*, *184*(3), 199–223. https://doi.org/10.2113/gssgfbull.184.3.199

Hacker, B. R. (1996). Eclogite formation and the rheology, buoyancy, seismicity, and H_2O content of oceanic crust. In G. E. Bebout, D. W. Scholl, S. H. Kirby, & J. P. Platt (Eds.), *Subduction: Top to bottom* (pp. 337–346). American Geophysical Union. https://doi.org/10.1029/GM096p0337

Hacker, B. R., Kelemen, P. B., & Behn, M. D. (2015). Continental lower crust. *Annual Review of Earth and Planetary Sciences*, *43*(1h), 167–205. https://doi.org/10.1146/annurev-earth-050212-124117

Handy, M. R., Schmid, S. M., Bousquet, R., Kissling, E., & Bernoulli, D. (2010). Reconciling plate-tectonic reconstructions of Alpine Tethys with the geological-geophysical record of spreading and subduction in the Alps. *Earth-Science Reviews*, *102*(3–4), 121–158. https://doi.org/10.1016/j.earscirev.2010.06.002

Herman, F., Copeland, P., Avouac, J. P., Bollinger, L., Maheo, G., Le Fort, P., et al. (2010). Exhumation, crustal deformation, and thermal structure of the Nepal Himalaya derived from the inversion of thermochronological and thermobarometric data and modeling of the topography. *Journal of Geophysical Research*, *115*(B6). https://doi.org/10.1029/2008jb006126

Hilley, G. E., Strecker, M. R., & Ramos, V. A. (2004). Growth and erosion of fold-and-thrust belts with an application to the Aconcagua fold-and-thrust belt, Argentina. *Journal of Geophysical Research*, *109*(B1). https://doi.org/10.1029/2002jb002282

Hu, X. M., Garzanti, E., Moore, T., & Raffi, I. (2015). Direct stratigraphic dating of India-Asia collision onset at the Selandian (middle Paleocene, 59 ± 1 Ma). *Geology*, *43*(10), 859–862. https://doi.org/10.1130/G36872.1

Huangfu, P. P., Li, Z. H., Gerya, T., Fan, W. M., Zhang, K. J., Zhang, H., & Shi, Y. L. (2018). Multi-terrane structure controls the contrasting lithospheric evolution beneath the western and central-eastern Tibetan Plateau. *Nature Communications*, *9*. https://doi.org/10.1038/s41467-018-06233-x

Huismans, R. S., & Beaumont, C. (2003). Symmetric and asymmetric lithospheric extension: Relative effects of frictional-plastic and viscous strain softening. *Journal of Geophysical Research*, *108*(B10). https://doi.org/10.1029/2002jb002026

Hyndman, R. D., Currie, C. A., & Mazzotti, S. P. (2005). Subduction zone backarcs, mobile belts, and orogenic heat. *Geological Society of America Today*, *15*(2), 4–10. https://doi.org/10.1130/1052-5173(2005)015⟨4:SZBMBA⟩2.0.CO;2

Iaffa, D. N., Sabat, F., Muñoz, J. A., Mon, R., & Gutierrez, A. A. (2011). The role of inherited structures in a foreland basin evolution. The Metan Basin in NW Argentina. *Journal of Structural Geology*, *33*(12), 1816–1828. https://doi.org/10.1016/j.jsg.2011.09.005

Jamieson, R. A., & Beaumont, C. (2013). On the origin of orogens. *Geological Society of America Bulletin*, *125*(11–12), 1671–1702. https://doi.org/10.1130/B30855.1

Jammes, S., & Huismans, R. S. (2012). Structural styles of mountain building: Controls of lithospheric rheologic stratification and extensional inheritance. *Journal of Geophysical Research: Solid Earth*, *117*(B10). https://doi.org/10.1029/2012jb009376

Jammes, S., Manatschal, G., Lavier, L., & Masini, E. (2009). Tectonosedimentary evolution related to extreme crustal thinning ahead of a propagating ocean: Example of the western Pyrenees. *Tectonics*, *28*(4). https://doi.org/10.1029/2008tc002406

Kapp, P., & DeCelles, P. G. (2019). Mesozoic-Cenozoic geological evolution of the Himalayan-Tibetan orogen and working tectonic hypotheses. *American Journal of Science*, *319*(3), 159–254. https://doi.org/10.2475/03.2019.01

Kapp, P., DeCelles, P. G., Gehrels, G. E., Heizier, M., & Ding, L. (2007). Geological records of the Lhasa-Qiangtang and Indo-Asian collisions in the Nima area of central Tibet. *Geological Society of America Bulletin*, *119*(7–8), 917–932. https://doi.org/10.1130/B26033.1

Kapp, P., Murphy, M. A., Yin, A., Harrison, T. M., Ding, L., & Guo, J. H. (2003). Mesozoic and Cenozoic tectonic evolution of the Shiquanhe area of western Tibet. *Tectonics*, *22*(4). https://doi.org/10.1029/2001tc001332

Kapp, P., Yin, A., Harrison, T. M., & Ding, L. (2005). Cretaceous-Tertiary shortening, basin development, and volcanism in central Tibet. *Geological Society of America Bulletin*, *117*(7–8), 865–878. https://doi.org/10.1130/B25595.1

Karato, S., & Wu, P. (1993). Rheology of the upper mantle: A synthesis. *Science*, *260*(5109), 771–778. https://doi.org/10.1126/science.260.5109.771

Katayama, I., & Karato, S. I. (2008). Low-temperature, high-stress deformation of olivine under water-saturated conditions. *Physics of the Earth and Planetary Interiors*, *168*(3–4), 125–133. https://doi.org/10.1016/j.pepi.2008.05.019

Kelly, S., Beaumont, C., & Butler, J. P. (2020). Inherited terrane properties explain enigmatic post-collisional Himalayan-Tibetan evolution. *Geology*, *1*, 8–14. https://doi.org/10.1130/g46701.1

Kelly, S., Butler, J. P., & Beaumont, C. (2016). Continental collision with a sandwiched accreted terrane: Insights into Himalayan-Tibetan lithospheric mantle tectonics? *Earth and Planetary Science Letters*, *455*, 176–195. https://doi.org/10.1016/j.epsl.2016.08.039

Lavé, J., & Avouac, J. P. (2001). Fluvial incision and tectonic uplift across the Himalayas of central Nepal. *Journal of Geophysical Research*, *106*(B11), 26561–26591. https://doi.org/10.1029/2001jb000359

Li, Z. H., Liu, M. A., & Gerya, T. (2016). Lithosphere delamination in continental collisional orogens: A systematic numerical study. *Journal of Geophysical Research: Solid Earth*, *121*(7), 5186–5211. https://doi.org/10.1002/2016jb013106

Liao, J., & Gerya, T. (2017). Partitioning of crustal shortening during continental collision: 2-D thermomechanical modeling. *Journal of Geophysical Research: Solid Earth*, *122*(1), 592–606. https://doi.org/10.1002/2016jb013398

Liao, J., Gerya, T., & Malosa, M. G. (2018). 3D modeling of crustal shortening influenced by along-strike lithological changes: Implications for continental collision in the Western and Central Alps. *Tectonophysics*, *746*, 425–438. https://doi.org/10.1016/j.tecto.2018.01.031

Liu, D., Zhao, Z. D., Zhu, D. C., Niu, Y. L., DePaolo, D. J., Harrison, T. M., et al. (2014). Postcollisional potassic and ultrapotassic rocks in southern Tibet: Mantle and crustal origins in response to India-Asia collision and convergence. *Geochimica et Cosmochimica Acta*, *143*, 207–231. https://doi.org/10.1016/j.gca.2014.03.031

Long, S., McQuarrie, N., Tobgay, T., & Grujic, D. (2011). Geometry and crustal shortening of the Himalayan fold-thrust belt, eastern and central Bhutan. *Geological Society of America Bulletin*, *123*(7–8), 1427–1447. https://doi.org/10.1130/B30203.1

Mackwell, S. J., Zimmerman, M. E., & Kohlstedt, D. L. (1998). High-temperature deformation of dry diabase with application to tectonics on Venus. *Journal of Geophysical Research*, *103*(B1), 975–984. https://doi.org/10.1029/97JB02671

Molnar, P., Boos, W. R., & Battisti, D. S. (2010). Orographic controls on climate and paleoclimate of Asia: Thermal and mechanical roles for the Tibetan Plateau. *Annual Review of Earth and Planetary Sciences*, *38*(38), 77–102. https://doi.org/10.1146/annurev-earth-040809-152456

Molnar, P., & Lyon-Caen, H. (1988). Some simple physical aspects of the support, structure, and evolution of mountain belts. *Geological Society of America Special Paper*, *218*, 179–207. https://doi.org/10.1130/SPE218-p179

Mouthereau, F., Filleaudeau, P. Y., Vacherat, A., Pik, R., Lacombe, O., Fellin, M. G., et al. (2014). Placing limits to shortening evolution in the Pyrenees: Role of margin architecture and implications for the Iberia/Europe convergence. *Tectonics*, *33*(12), 2283–2314. https://doi.org/10.1002/2014tc003663

Muñoz, J. A. (1992). Evolution of a continental collision belt: ECORS-Pyrenees crustal balanced cross-section *Thrust tectonics* (pp. 235–246). Dordrecht: Springer.

Muñoz, J. A. (2019). Deformation and structure in the Northern Iberian margin (Pyrenees s.l.). In C. Quesada & J. Oliveira (Eds.), *The geology of Iberia: A geodynamic approach*. Cham: Springer.

Nabelek, J., Hetenyi, G., Vergne, J., Sapkota, S., Kafle, B., Jiang, M., et al. (2009). Underplating in the Himalaya-Tibet collision zone revealed by the Hi-CLIMB experiment. *Science*, *325*(5946), 1371–1374. https://doi.org/10.1126/science.1167719

Negredo, A. M., Replumaz, A., Villasenor, A., & Guillot, S. (2007). Modeling the evolution of continental subduction processes in the Pamir-Hindu Kush region. *Earth and Planetary Science Letters*, *259*(1–2), 212–225. https://doi.org/10.1016/j.epsl.2007.04.043

Owens, T. J., & Zandt, G. (1997). Implications of crustal property variations for models of Tibetan Plateau evolution. *Nature*, *387*(6628), 37–43. https://doi.org/10.1038/387037a0

Poudjom Djomani, Y. H., O'Reilly, S. Y., Griffin, W. L., & Morgan, P. (2001). The density structure of subcontinental lithosphere through time. *Earth and Planetary Science Letters*, *184*(3–4), 605–621.

Pysklywec, R. N., & Beaumont, C. (2004). Intraplate tectonics: Feedback between radioactive thermal weakening and crustal deformation driven by mantle lithosphere instabilities. *Earth and Planetary Science Letters*, *221*(1–4), 275–292. https://doi.org/10.1016/S0012-821x(04)00098-6

Replumaz, A., Negredo, A. M., Guillot, S., van der Beek, P., & Villasenor, A. (2010). Crustal mass budget and recycling during the India/Asia collision. *Tectonophysics*, *492*(1–4), 99–107. https://doi.org/10.1016/j.tecto.2010.05.023

Replumaz, A., & Tapponnier, P. (2003). Reconstruction of the deformed collision zone between India and Asia by backward motion of lithospheric blocks. *Journal of Geophysical Research*, *108*(B6). https://doi.org/10.1029/2001jb000661

Robinson, D. M. (2008). Forward modeling the kinematic sequence of the central Himalayan thrust belt, western Nepal. *Geosphere*, *4*(5), 785–801. https://doi.org/10.1130/Ges00163.1

Rohrmann, A., Kapp, P., Carrapa, B., Reiners, P. W., Guynn, J., Ding, L., & Heizler, M. (2012). Thermochronologic evidence for plateau formation in central Tibet by 45 Ma. *Geology*, *40*(2), 187–190. https://doi.org/10.1130/G32530.1

Rosenberg, C. L., & Kissling, E. (2013). Three-dimensional insight into Central-Alpine collision: Lower-plate or upper-plate indentation? *Geology*, *41*(12), 1219–1222. https://doi.org/10.1130/G34584.1

Ruh, J. B., Gerya, T., & Burg, J.-P. (2017). Toward 4D modeling of orogenic belts: Example from the transpressive Zagros Fold Belt. *Tectonophysics*, *702*(Supplement C), 82–89. https://doi.org/10.1016/j.tecto.2015.09.035

Sandiford, M., & Powell, R. (1990). Some isostatic and thermal consequences of the vertical strain geometry in convergent orogens. *Earth and Planetary Science Letters*, *98*(2), 154–165. https://doi.org/10.1016/0012-821x(90)90056-4

Schmalholz, S. M., Medvedev, S., Lechmann, S. M., & Podladchikov, Y. (2014). Relationship between tectonic overpressure, deviatoric stress, driving force, isostasy and gravitational potential energy. *Geophysical Journal International*, *197*(2), 680–696. https://doi.org/10.1093/gji/ggu040

Schmid, S. M., Fugenschuh, B., Kissling, E., & Schuster, R. (2004). Tectonic map and overall architecture of the Alpine orogen. *Eclogae Geologicae Helvetiae*, *97*(1), 93–117. https://doi.org/10.1007/s00015-004-1113-x

Schmid, S. M., & Kissling, E. (2000). The arc of the western Alps in the light of geophysical data on deep crustal structure. *Tectonics*, *19*(1), 62–85. https://doi.org/10.1029/1999tc900057

Schmid, S. M., Kissling, E., Diehl, T., van Hinsbergen, D. J. J., & Molli, G. (2017). Ivrea mantle wedge, arc of the Western Alps, and kinematic evolution of the Alps-Apennines orogenic system. *Swiss Journal of Geosciences*, *110*(2), 581–612. https://doi.org/10.1007/s00015-016-0237-0

Schmid, S. M., Pfiffner, O. A., Froitzheim, N., Schonborn, G., & Kissling, E. (1996). Geophysical-geological transect and tectonic evolution of the Swiss-Italian Alps. *Tectonics*, *15*(5), 1036–1064. https://doi.org/10.1029/96tc00433

Schurr, B., Rietbrock, A., Asch, G., Kind, R., & Oncken, O. (2006). Evidence for lithospheric detachment in the central Andes from local earthquake tomography. *Tectonophysics*, *415*(1–4), 203–223. https://doi.org/10.1016/j.tecto.2005.12.007

Sibuet, J. C., Srivastava, S. P., & Spakman, W. (2004). Pyrenean orogeny and plate kinematics. *Journal of Geophysical Research*, *109*(B8). https://doi.org/10.1029/2003jb002514

Sommaruga, A. (1999). Decollement tectonics in the Jura foreland fold-and-thrust belt. *Marine and Petroleum Geology*, *16*(2), 111–134. https://doi.org/10.1016/S0264-8172(98)00068-3

Stampfli, G. M., Mosar, J., Marquer, D., Marchant, R., Baudin, T., & Borel, G. (1998). Subduction and obduction processes in the Swiss Alps. *Tectonophysics*, *296*(1–2), 159–204. https://doi.org/10.1016/S0040-1951(98)00142-5

Stock, J. D., & Montgomery, D. R. (1999). Geologic constraints on bedrock river incision using the stream power law. *Journal of Geophysical Research*, *104*(B3), 4983–4993.

Stockmal, G. S., Beaumont, C., Nguyen, M., & Lee, B. (2007). Mechanics of thin-skinned fold-and-thrust belts: Insights from numerical models In J. W. Sears, T. A. Harms, & C. A. Evenchick (Eds.), Whence the Mountains? Inquiries into the Evolution of Orogenic Systems: A Volume in Honor of Raymond A. Price (Vol. 433). Geological Society of America. https://doi.org/10.1130/2007.2433(04)

Stolar, D. B., Roe, G. H., & Willett, S. D. (2007). Controls on the patterns of topography and erosion rate in a critical orogen. *Journal of Geophysical Research*, *112*(F4). https://doi.org/10.1029/2006jf000713

Stolar, D. B., Willett, S. D., & Roe, G. H. (2006). Climatic and tectonic forcing of a critical orogen. *Special Papers-Geological Society of America*, *398*, 241. https://doi.org/10.1130/2006.2398(14)

Teixell, A., Labaume, P., Ayarza, P., Espurt, N., de Saint Blanquat, M., & Lagabrielle, Y. (2018). Crustal structure and evolution of the Pyrenean-Cantabrian belt: A review and new interpretations from recent concepts and data. *Tectonophysics*, *724*, 146–170. https://doi.org/10.1016/j.tecto.2018.01.009

Thieulot, C. (2011). FANTOM: Two- and three-dimensional numerical modelling of creeping flows for the solution of geological problems. *Physics of the Earth and Planetary Interiors*, *188*(1–2), 47–68. https://doi.org/10.1016/j.pepi.2011.06.011

Thieulot, C., Steer, P., & Huismans, R. S. (2014). Three-dimensional numerical simulations of crustal systems undergoing orogeny and subjected to surface processes. *Geochemistry, Geophysics, Geosystems*, *15*(12), 4936–4957. https://doi.org/10.1002/2014gc005490

Tsenn, M. C., & Carter, N. L. (1987). Upper limits of power law creep of rocks. *Tectonophysics*, *136*(1–2), 1–26. https://doi.org/10.1016/0040-1951(87)90332-5

Tugend, J., Manatschal, G., Kusznir, N. J., Masini, E., Mohn, G., & Thinon, I. (2014). Formation and deformation of hyperextended rift systems: Insights from rift domain mapping in the Bay of Biscay-Pyrenees. *Tectonics*, *33*(7), 1239–1276. https://doi.org/10.1002/2014tc003529

Turcotte, D. L., & Schubert, G. (1982). *Geodynamics*. New York, NY: John Wiley.

Ueda, K., Willett, S. D., Gerya, T., & Ruh, J. (2015). Geomorphological-thermo-mechanical modeling: Application to orogenic wedge dynamics. *Tectonophysics*, *659*, 12–30. https://doi.org/10.1016/j.tecto.2015.08.001

van der Beek, P., Van Melle, J., Guillot, S., Pecher, A., Reiners, P. W., Nicolescu, S., & Latif, M. (2009). Eocene Tibetan Plateau remnants preserved in the northwest Himalaya. *Nature Geoscience*, *2*(5), 364–368. https://doi.org/10.1038/Ngeo503

Vanderhaeghe, O., Medvedev, S., Fullsack, P., Beaumont, C., & Jamieson, R. A. (2003). Evolution of orogenic wedges and continental plateaux: Insights from crustal thermal-mechanical models overlying subducting mantle lithosphere. *Geophysical Journal International*, *153*(1), 27–51. https://doi.org/10.1046/j.1365-246X.2003.01861.x

Vogt, K., Willingshofer, E., Matenco, L., Sokoutis, D., Gerya, T., & Cloetingh, U. S. (2018). The role of lateral strength contrasts in orogenesis: A 2D numerical study. *Tectonophysics*, *746*, 549–561. https://doi.org/10.1016/j.tecto.2017.08.010

Volkmer, J. E., Kapp, P., Guynn, J. H., & Lai, Q. Z. (2007). Cretaceous-Tertiary structural evolution of the north central Lhasa terrane, Tibet. *Tectonics*, *26*(6). https://doi.org/10.1029/2005tc001832

Wang, C. S., Dai, J. G., Zhao, X. X., Li, Y. L., Graham, S. A., He, D. F., et al. (2014). Outward-growth of the Tibetan Plateau during the Cenozoic: A review. *Tectonophysics*, *621*, 1–43. https://doi.org/10.1016/j.tecto.2014.01.036

Whipple, K. X., & Meade, B. J. (2004). Controls on the strength of coupling among climate, erosion, and deformation in two-sided, frictional orogenic wedges at steady state. *Journal of Geophysical Research*, *109*(F1). https://doi.org/10.1029/2003jf000019

Whipple, K. X., & Meade, B. J. (2006). Orogen response to changes in climatic and tectonic forcing. *Earth and Planetary Science Letters*, *243*(1), 218–228. https://doi.org/10.1016/j.epsl.2005.12.022

Whipple, K. X., & Tucker, G. E. (1999). Dynamics of the stream-power river incision model: Implications for height limits of mountain ranges, landscape response timescales, and research needs. *Journal of Geophysical Research*, *104*(B8), 17661–17674. https://doi.org/10.1029/1999jb900120

Willett, S. D. (1999). Orogeny and orography: The effects of erosion on the structure of mountain belts. *Journal of Geophysical Research*, *104*(B12), 28957–28981. https://doi.org/10.1029/1999jb900248

Willett, S. D., & Beaumont, C. (1994). Subduction of Asian lithospheric mantle beneath Tibet inferred from models of continental collision. *Nature*, *369*(6482), 642–645. https://doi.org/10.1038/369642a0

Willett, S. D., Beaumont, C., & Fullsack, P. (1993). Mechanical model for the tectonics of doubly vergent compressional orogens. *Geology*, *21*(4), 371–374. https://doi.org/10.1130/0091-7613(1993)021⟨0371:Mmftto⟩2.3.Co;2

Willett, S. D., & Brandon, M. T. (2002). On steady states in mountain belts. *Geology*, *30*(2), 175–178. https://doi.org/10.1130/0091-7613(2002)030⟨0175:Ossimb⟩2.0.Co;2

Willett, S. D., Slingerland, R., & Hovius, N. (2001). Uplift, shortening, and steady-state topography in active mountain belts. *American Journal of Science*, *301*(4–5), 455–485. https://doi.org/10.2475/ajs.301.4-5.455

Wilson, J. T. (1966). Did the Atlantic close and then re-open? *Nature*, *211*(5050), 676–681. https://doi.org/10.1038/211676a0

Wobus, C. W., Hodges, K. V., & Whipple, K. X. (2003). Has focused denudation sustained active thrusting at the Himalayan topographic front? *Geology*, *31*(10), 861–864. https://doi.org/10.1130/G19730.1

Wolf, S. G., & Huismans, R. S. (2019). Mountain Building or Backarc Extension in Ocean-Continent Subduction Systems: A Function of Backarc Lithospheric Strength and Absolute Plate Velocities. *Journal of Geophysical Research: Solid Earth*, *124*(7), 7461–7482. https://doi.org/10.1029/2018JB017171

Yi, Z. Y., Huang, B. C., Chen, J. S., Chen, L. W., & Wang, H. L. (2011). Paleomagnetism of early Paleogene marine sediments in southern Tibet, China: Implications to onset of the India-Asia collision and size of Greater India. *Earth and Planetary Science Letters*, *309*(1–2), 153–165. https://doi.org/10.1016/j.epsl.2011.07.001

Yin, A., & Harrison, T. M. (2000). Geologic evolution of the Himalayan-Tibetan orogen. *Annual Review of Earth and Planetary Sciences*, *28*(1), 211–280. https://doi.org/10.1146/annurev.earth.28.1.211

Yuan, X., Braun, J., Guerit, L., Rouby, D., & Cordonnier, G. (2019). A new efficient method to solve the stream power law model taking into account sediment deposition. *Journal of Geophysical Research: Earth Surface*, *124*(6), 1346–1365. https://doi.org/10.1029/2018jf004867

Zhou, S. H., & Sandiford, M. (1992). On the stability of isostatically compensated mountain belts. *Journal of Geophysical Research*, *97*(B10), 14207–14221. https://doi.org/10.1029/92jb01091